MAGNETOGASDYNAMIC FLOW ACCELERATION IN A SCRAMJET NOZZLE

THESIS

Brian H. Harrington, Ensign, USN

AFIT/GAE/ENY/04-J03

DEPARTMENT OF THE AIR FORCE

AIR UNIVERSITY

AIR FORCE INSTITUTE OF TECHNOLOGY

Wright-Patterson Air Force Base, Ohio

Approved for public release; distribution unlimited

The views expressed in this thesis are those of the author and do not reflect the official policy or position of the United States Navy, the United States Air Force, Department of Defense, or the United States Government.

AFIT/GAE/ENY/04-J03

MAGNETOGASDYNAMIC FLOW ACCELERATION IN A SCRAMJET NOZZLE

THESIS

Presented to the Faculty of the

Department of Aeronautics and Astronautics

Graduate School of Engineering and Management

Air Force Institute of Technology

Air University

Air Education and Training Command

in Partial Fulfillment of the Requirements for the

Degree of Master of Science in Aeronautical Engineering

Brian H. Harrington, B.S.

Ensign, USN

June, 2004

Approved for public release; distribution unlimited

AFIT/GAE/ENY/04-J03

MAGNETOGASDYNAMIC FLOW ACCELERATION IN A SCRAMJET NOZZLE

Brian H. Harrington, B.S.

Ensign, USN

Approved:

// Signed //	03 Jun 04
Maj. Richard J. McMullan, Ph.D. Thesis Advisor	Date
// Signed //	03 Jun 04
Lt. Col. Raymond C. Maple, Ph.D. Committee Member	Date
// Signed //	03 Jun 04
Jose Camberos, Ph.D. Committee Member	Date

AFIT/GAE/ENY/04-J03

Abstract

The effect of magnetogasdynamic (MGD) interactions on flow acceleration and thrust in a scramjet accelerator/nozzle are examined numerically at a free-stream flight condition of Mach 8. The parameters of conductivity pattern and load factor are varied in both inviscid and viscous flow regimes with the intent of increasing axial force exerted on the flow through a scramjet accelerator. The numerical code solves the Navier-Stokes equations with additional source terms for the MGD forces and energy interactions. An accelerating Lorentz force is applied to the flow resulting from a constant magnetic field and an electric field produced by two continuous side wall electrodes. The specific thrust across the accelerator/nozzle is improved in the MGD solutions over the non-MGD solutions when the load factor is increased and an electron beam type ionization pattern is used. The largest increase in specific thrust is observed in viscous and inviscid flow regimes with a load factor of 1.8 producing 226% and 154% thrust increases, respectively. Flows showing increases in specific thrust with higher load factors also show significant increases in temperature due to the energy interaction term.

Acknowledgements

First I thank Maj. McMullan for giving of his time and expertise to help me succeed in completing this project. Without his help and guidance I could not have completed so much in such a short time. I thank all those at AFRL who helped me along the way, including Dr. Camberos for providing me with a base in magnetogasdynamics. I also thank Dr. Gaitonde of AFRL who was so supportive in helping to implement his computational code. I hope that this work in some way furthers his study into magnetogasdynamics. I want to recognize Dr. John Schmisseur of AFOSR/NA for the funding support for this research. I also thank Lt. Col. Maple and Lt. Col. Hughson for teaching me the basics of CFD and helping me to appreciate a part of this project that I became so involved in. Thank you to Capt. Earp who passed this research on to me and I wish luck to Maj. Lindsey who will be continuing this research. Most of all, thanks to my family and friends who continue to encourage and support me in all that I do. Finally, I thank the other Navy students for their continuing support, without whom I may still be wandering the halls of AFIT looking for my first class.

Brian H. Harrington

Table of Contents

Page

Abstract iv

Acknowledgements v

List of Figures viii

List of Tables xi

List of Symbols xii

List of Abbreviations xvi

1. Introduction 1-1

1.1 Scramjet Research 1-3

1.2 Magnetogasdynamic Flow Control 1-5

1.3 Current Research 1-9

2. Governing Equations 2-1

2.0.1 The Vector Form Navier-Stokes Equations . . 2-1

2.0.2 Ideal Gas Law 2-2

2.1 Maxwell Equations 2-2

2.1.1 Ohm's Law 2-3

2.1.2 Constitutive Relations 2-4

2.1.3 Magnetogasdynamic Assumptions 2-4

2.1.4 Maxwell Equations for Magnetogasdynamic Flow 2-5

2.2 Magnetogasdynamic Equations 2-5

2.2.1 Non-dimensionalizing the Magnetogasdynamic Equations 2-6

Page

3. Computational Set-Up 3-1

3.1 MGD 3-D Computational Code 3-1

3.2 Thrust Calculation Model 3-1

3.3 Computational Domain 3-3

3.4 Computational Parameters 3-6

3.5 Computational Cases 3-9

4. Results 4-1

4.1 Baseline Cases 4-1

4.1.1 Case 1: Inviscid 4-1

4.1.2 Case 2: Viscous 4-3

4.2 MGD Results: Conductivity Pattern 1 4-7

4.2.1 Case 3: Inviscid Load Factor 1.4 4-7

4.2.2 Case 4: Inviscid Load Factor 1.2 4-13

4.2.3 Case 5: Inviscid Load Factor 1.8 4-14

4.2.4 Case 6: Viscous Load Factor 1.4 4-16

4.2.5 Case 7: Viscous Load Factor 1.8 4-19

4.3 MGD Results: Conductivity Pattern 2 4-23

4.3.1 Case 8: Inviscid Load Factor 1.4 4-26

4.4 Load Factor Effects 4-27

4.5 Thrust 4-29

5. Conclusions 5-1

Bibliography BIB-1

Vita VITA-1

List of Figures

Figure		Page
1.1.	NASA's X-43A hypersonic vehicle[5].	1-4
1.2.	Simplified Magneto-Plasma-Chemical Engine (MPCE) [19]. .	1-8
1.3.	Simplified Mach 8 scramjet model design[7].	1-11
3.1.	Preliminary design used in the grid convergence study.	3-3
3.2.	Three dimensional MGD accelerator geometry.	3-4
3.3.	Three dimensional inviscid mesh design.	3-5
3.4.	Three dimensional viscous mesh design.	3-6
3.5.	MGD accelerator conductivity pattern 1.	3-8
3.6.	MGD accelerator conductivity pattern 2.	3-8
3.7.	Schematic of an accelerating Lorentz force vector.	3-9
4.1.	Case 1 - 3D inviscid results: Mach number.	4-2
4.2.	Case 1 - 2D inviscid contour lines: Pressure. (top: x-y midplane, bottom: x-z midplane)	4-3
4.3.	Case 1 - 2D inviscid contour lines: Temperature. (top: x-y midplane, bottom: x-z midplane)	4-4
4.4.	Case 1 - 2D inviscid contour lines: Velocity Magnitude. (top: x-y midplane, bottom: x-z midplane)	4-4
4.5.	Case 2 - 3D viscous results: Mach number.	4-5
4.6.	Case 2 - 2D viscous contour lines: Pressure. (top: x-y midplane, bottom: x-z midplane)	4-6
4.7.	Case 2 - 2D viscous contour lines: Temperature. (top: x-y midplane, bottom: x-z midplane)	4-6
4.8.	Case 2 - Viscous boundary layer profile.	4-7
4.9.	Case 3 - 2D electric field. (x-z midplane)	4-8

Figure Page

4.10. Case 3 - Lorentz vectors. (top: x-y midplane, bottom: x-z midplane) 4-9

4.11. Case 3 - 3D inviscid results: Mach number. 4-10

4.12. Case 3 - 3D inviscid results: Temperature. 4-11

4.13. Case 3 - 2D inviscid contour lines: Temperature. (top: x-y side plane, middle: x-y midplane, bottom: x-z midplane) 4-11

4.14. Case 3 - 2D inviscid contour lines: Pressure. (top: x-y midplane, bottom: x-z midplane) 4-12

4.15. Case 3 - 2D inviscid contour lines: Velocity. (top: x-y midplane, bottom: x-z midplane) 4-12

4.16. Case 4 - Lorentz vectors. (top: x-y midplane, bottom: x-z midplane) 4-13

4.17. Case 4 - 2D inviscid contour lines: Velocity. (top: x-y midplane, bottom: x-z midplane) 4-14

4.18. Case 4 - 2D inviscid contour lines: Temperature. (top: x-y side plane, middle: x-y midplane, bottom: x-z midplane) 4-15

4.19. Case 5 - Lorentz vectors. (top: x-y midplane, bottom: x-z midplane) 4-15

4.20. Case 5 - 2D inviscid contour lines: Velocity. (top: x-y midplane, bottom: x-z midplane) 4-16

4.21. Case 5 - 2D inviscid contour lines: Temperature. (top: x-y side plane, middle: x-y midplane, bottom: x-z midplane) 4-17

4.22. Case 6 - 3D Lorentz force vectors. 4-18

4.23. Case 6 - 2D Lorentz force vectors. (top: x-y midplane, bottom: x-z midplane) 4-18

4.24. Case 6 - 3D flow field contours. 4-20

4.25. Case 6 - 2D viscous contour lines: Velocity. (top: x-y midplane, bottom: x-z midplane) 4-21

4.26. Case 6 - 2D viscous contour lines: Temperature. (top: x-y midplane, bottom: x-z midplane) 4-21

Figure Page

4.27. Case 7 - 3D Lorentz force vectors. 4-22

4.28. Case 7 - 2D Lorentz force vectors. (top: x-y midplane, bottom: x-z midplane) 4-22

4.29. Case 7 - 3D flow field contours. 4-24

4.30. Case 7 - 2D viscous contour lines: Velocity. (top: x-y midplane, bottom: x-z midplane) 4-25

4.31. Case 7 - 2D viscous contour lines: Temperature. (top: x-y midplane, bottom: x-z midplane) 4-25

4.32. Case 8 - 2D Lorentz force vectors. (top: x-y side plane, middle: x-y midplane, bottom: x-z midplane) 4-26

4.33. Case 8 - Scaled Lorentz force vectors and electrode wall profile. (top: x-z midplane, bottom: electrode wall profile) 4-27

4.34. Case 8 - 2D inviscid contour lines: Velocity. (top: x-y midplane, bottom: x-z midplane) 4-28

4.35. Case 8 - 2D inviscid contour lines: Temperature. (top: x-y midplane, bottom: x-z midplane) 4-28

4.36. Lorentz vectors for Cases 3, 4 and 5. 4-30

List of Tables

Table		Page
3.1.	Freestream and MGD Accelerator Inlet Conditions.	3-7
3.2.	Test Case Parameters.	3-10
4.1.	Summary of Test Case Exit Plane Results.	4-31

List of Symbols

Roman symbols:

A	area
a	sound speed
B	magnetic flux density
B_0	magnitude of the magnetic flux density
c_p	constant pressure specific heat
D	electric flux density
E	electric field or viscous/inviscid component of the flux vector in the x- or ξ-direction
E_0	magnitude of the applied electric field
$\mathbf{E}$	flux vector in the x- or ξ-direction
e	energy
F	force or viscous/inviscid component of the flux vector in the y- or η-direction
$\mathbf{F}$	flux vector in y- or η-direction
f	force density
G	viscous/inviscid component of the flux vector in the z- or ζ-direction
$\mathbf{G}$	flux vector in z- or ζ-direction
H	magnetic field
h	enthalpy
I	axial impulse function
j	conduction current density
$\mathcal{K}$	load factor
L	reference length
$\dot{m}$	mass flow rate
M	Mach number
Mm	magnetic Mach number

Pm	magnetic Prandtl number
Pr	Prandtl number
p	pressure
$\mathcal{Q}$	interaction parameter
q	heat flux
Re	Reynolds number
Rm	magnetic Reynolds number
S	source vector
Sa	mass flow rate specific thrust
T	temperature
t	time
U	conservative variable vector
u	component of velocity in the x-direction
V	velocity
v	component of velocity in the y-direction
w	component of velocity in the z-direction
x	coordinate direction of the principle axis
y	coordinate direction of the principle axis
z	coordinate direction of the principle axis

Greek symbols:

ϵ	permittivity
γ	ratio of specific heats
κ	thermal conductivity
μ	permeability or viscosity
ν	kinematic viscosity
ρ	density
ρ_e	charge unit volume
σ	conductivity
τ	stress tensor
ϕ	electric potential
∂	partial differential operator
∇	gradient operator

Subscripts:

0	freestream value or reference location
e	electromagnetic
f	fluid
i	inviscid, index notation, or tensorial component
j, k	index notation or tensorial component
t	total condition
v	viscous
x	x-component or differentiation with respect to x
y	y-component or differentiation with respect to y
z	z-component or differentiation with respect to z

Superscripts:

$'$	rest frame
$*$	dimensionless quantity
$\bar{}$	vector quantity
$\rightarrow$	vector quantity

Constants:

$\mathbf{c}$	speed of light *in vacuum*	$2.998 \times 10^8 \frac{m}{s}$
$\mathcal{R}$	universal gas constant	$287 \ \frac{J}{kgK}$
$\epsilon_{0,e}$	electric constant (permittivity of free space)	$8.854 \times 10^{-12} \frac{F}{m}$
$\mu_{0,e}$	magnetic constant (permeability of free space)	$4\pi \times 10^{-7} \frac{H}{m}$

List of Abbreviations

Abbreviation		Page
CFD	··· Computational Fluid Dynamics	1-2
MGD	··· Magnetogasdynamic	1-5
MPCE	··· Magneto Plasma Chemical Engine	1-7
VAAC	··· Air Vehicles Directorate Computational Sciences Branch	1-10
AFRL	··· Air Force Research Laboratory	1-11
MFM	··· Magnetofluidmechanics	2-4
MUSCL	··· Monotone Upstream-centered Schemes for Conservation Laws	3-1

MAGNETOGASDYNAMIC FLOW ACCELERATION IN A SCRAMJET NOZZLE

1. Introduction

Since the Wright Brother's first powered flight on December 17, 1903, aviators and engineers have explored the new frontier of flight and sought after new aircraft that seem to defy the laws of nature. It seems engineers have adopted the Olympic maxim "citus, altius, fortius" as they push the limits of aircraft and aviation "faster, higher, and stronger." Despite obvious risks and uncertainties, pilots jump at the chance to push the bounds of flight. The famous pioneer in aviation history, Chuck Yeager, was assigned to test pilot the X-1 and became the first person to fly beyond the speed of sound on October 14, 1947. At the time, the flight was riddled with uncertainty and many of those involved did not know what to expect. Looking back on the event 50 years later Yeager said, "We had no idea what was going to happen . . . you're in an area where very little is known. They had no wind tunnel data, nothing, and everything was trial and error."[30]

At present, aviation is once again on the cutting edge of propulsion technology, exploring hypersonic flow regimes and attempting to make sustained hypersonic flight a reality. Rockets and ramjet engines have been the cornerstone of supersonic flight reaching speeds up to Mach 6, but they have effectively reached the limit of their operability. The future of hypersonic flight is looking toward the supersonic combustion ramjet, or scramjet, engine to propel them into the next phase of aviation evolution. Like breaking the sound barrier, there are many unknowns in the development of this new technology, but fortunately engineers no longer have to rely on trial and error for progress to be made. Increasingly Computational Fluid

Dynamics (CFD) is playing a larger role in testing and developing engine and aircraft designs. Today when scramjet technology is flight tested, its designs are based on many hours of ground tests and CFD evaluations, reducing the risk and cost of failure while increasing safety and the promise of success.

Sustained hypersonic flight, which has yet to happen, but surely will, has been a realistic desire for over half a century. At present, hypersonic flight is attained through either rocket propulsion or air-breathing engines called ramjets, but these are not new ideas. Patents on file show ramjet engines designed for supersonic flight as early as 1928, and since the flight of the X-1, many aircraft, spacecraft, and missiles have flown through Earth's atmosphere at supersonic and hypersonic speeds [12]. Still, as mentioned before, these methods seem to have met the limit of their application. When looking at sustained hypersonic flight, both propulsion systems have shortfalls that seem unavoidable.

Rockets have long been used to achieve supersonic and hypersonic speeds and have been instrumental in everything from missiles to the Space Shuttle launch. However, further advancements in rocket propulsion will yield only small improvements in performance, since rocket performance has been advanced close to its theoretical limits [26]. Rocket systems carry much larger propellant mass fractions since they must provide their own oxidizer, which is carried with them during the flight. The weight added by the oxidizer greatly reduces the payload the aircraft can carry, thus reducing its mission capabilities. Like many other engineering applications, rocket design is a trade off, and near Mach 6, the adverse effects of carrying the oxidizer begin to out weigh the benefits.

Air-breathing engines eliminate the additional weight and increase payload by using atmospheric oxygen as the oxidizer. Ramjets operate by slowing the oncoming flow to subsonic speeds in the combustor section [12]. The atmospheric oxygen is mixed with the fuel and ignited. However, ramjets too have their shortfalls. When approaching Mach 6, the drag associated with slowing the flow to subsonic levels

for combustion begins to make the thrust provided by the ramjet ineffective [26]. Again, the drag penalty paid to have subsonic flow begins to out weigh the thrust benefits in the design trade off. This means that ramjets have also approached their operational limits.

1.1 Scramjet Research

The next step in the evolution of hypersonic propulsion is the scramjet. As its name suggests, a scramjet operates much like a ramjet, only the combustion process is done at supersonic speeds. This overcomes both of the problems previously discussed with rockets and ramjets. Supersonic combustion reduces the drag associated with slowing the flow in the combustor, and an air-breathing engine eliminates the extra weight, increasing payload [12, 26]. Still, scramjet designs have many problems of their own. At present, scramjet designs are limited in their flight envelope and require a boost, most likely from a rocket, to get up to a speed great enough to sustain combustion [4, 15]. Supersonic combustion, shock structure control, and material limits all pose significant hurdles to designing a working scramjet with today's technology [3, 4, 21, 24, 26, 28]. That, however, has not stopped engineers from exploring the possibility of scramjet propulsion. Two of the most notable hypersonic programs are the University of Queensland's HyShot Flight Program, and NASA's Hyper-X Program.

The University of Queensland's HyShot Flight Program is one of several investigating the possibility of scramjet propulsion flight tests. The program has conducted two flight tests of which supersonic combustion was achieved on the second flight in July 2002 [15]. In their tests, the scramjet was propelled to an altitude of 330 km with the aid of a rocket. The rocket and engine were then directed back down and the second rocket stage was fired. This propelled the scramjet to a design Mach of 7.6 at an altitude between 35km and 23km. This allowed for 5 seconds of scramjet propulsion using hydrogen gas as the fuel.

The Hyshot team has encountered some difficulties unique to their test design. Due to their vertical trajectory during the launch, accelerations reach a peak of 60g before decaying to 30g which can cause the flight test to fail structurally in the first second of flight [15]. In addition, the scramjet has not been designed to produce a net thrust since the objectives of the experiment are to measure pressures in the combustor and thrust surfaces for comparison to tunnel data.

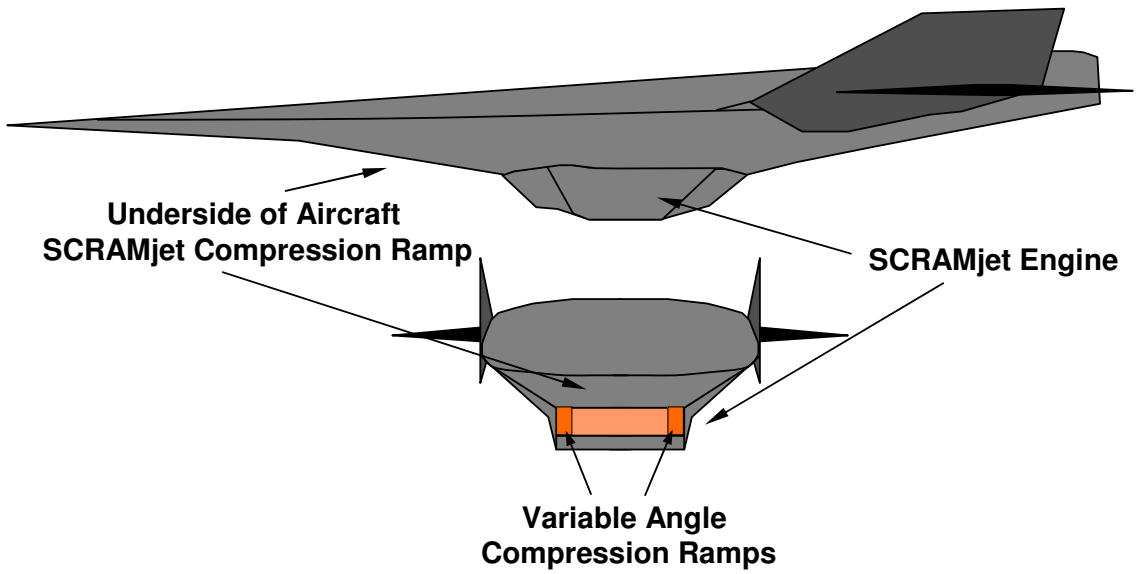

Figure 1.1 NASA's X-43A hypersonic vehicle[5].

One of the most successful scramjet programs to date has been NASA's $250 million Hyper-X Program which is responsible for the experimental X-43A hypersonic research vehicle shown in Figure 1.1 [31]. The X-43A is the first operational design to integrate the engine into the body of the aircraft and is not unlike many other scramjet aircraft designs. It is widely agreed that only when the engine is integrated with the airframe does engine performance have useful meaning [26]. In the X-43A, the underside of the aircraft is used as the compression ramp in the inlet and also as the thrust surface at the nozzle exit.

The Hyper-X program had it's first success when the X-43A completed its first successful flight on March 27, 2004 reaching Mach 7 at roughly 100,000 ft

altitude [31]. This flight marked the first supersonic flight powered by a non-rocket, air-breathing scramjet engine. However, due to problems in the present design, a feasible aircraft capable of sustained hypersonic flight may be delayed by several decades.

One of the most significant problems for the scramjet is efficient supersonic combustion, which has some inherent design difficulties which must be addressed before efficient supersonic propulsion can be obtained [3, 4, 21]. For example, supersonic combustor flow is much faster than flame propagation speed and the flame is blown out the back of the engine. To remedy this in the X-43A, engineers designed subsonic local flame-holders to sustain combustion, but at the price of increased drag to slow the flow to subsonic speeds [4]. In addition, introducing too much fuel to the combustor could increase the back pressure, causing the inlet shock train to be blown from the engine, resulting in unstart. Efficiency is also degraded when molecular dissociation, total pressure losses, and incomplete engine combustion are taken into account [28].

Engine cooling and aircraft stability are also design hurdles for engineers. The X-43A has an 800-lb. tungsten slab in the nose to move the center of gravity to within stability and control limits, which accounts for 29% of its gross weight [4]. Cooling will become a significant issue for flights longer than 10 seconds. In a program where efficiency is ultimately the goal, there are many modifications that must be made to the existing design, the greatest of which is efficient flow control and energy management in the overall aircraft design.

1.2 Magnetogasdynamic Flow Control

Due to the immense flow control problems that many designers have encountered, a significant number have turned to magnetogasdynamics (MGD) as a means to control the complex flow fields passing through a scramjet [2, 16, 17, 19, 21, 22, 23, 25, 27, 28, 29]. The principle force used in MGD flow control is the Lorentz

force, oriented to interact with a conductive flow. There are many MGD flow control applications, including shock location control for inlet mass capture [24], suppressing boundary layer transition, and enhancing fuel air mixing in the combustor [3]. More complex uses of MGD include withdrawing energy from the flow in the inlet to reduce the flow velocity using an MGD generator, and then inserting the energy back into the flow in the nozzle section to increase thrust using an MGD accelerator [1, 16, 17, 18, 19, 20, 29].

As expected, the concept of MGD flow control is not without its own setbacks and concerns. Present research has suggested the magnetic forces required to control the flow are on the order of 10 Tesla. The weight of super-conducting coil magnets for creating field strengths of that magnitude account for 85% of the MGD system weight. Research into new materials to reduce the magnet weight is vital to the success of MGD flow control on an aircraft [25].

Ensuring flow conductivity is another main problem that must be solved. At hypersonic flight conditions, conductivity of a flow is negligible to produce essential MGD interactions [1]. Some have suggested pre-ionizing the flow at the entrance of the scramjet, however Macheret shows some design problems with this method. If electron densities of about 10^{12} per cc minimally are required for MGD operation, plasma recombination is about 10-30 microseconds [22]. At a flow velocity of 500 to 2,000 meters per second, the conductivity of the flow would decay in just a few centimeters. Macheret's analysis also demonstrated that, with careful choice of parameters, electron beams could form stable, well controlled plasmas, potentially enabling a good level of generator performance. There are several possible processes for ionizing the flow, including electron beam ionization and high-voltage pulses from either DC or RF discharges. Many agree that of the available choices, the electron beam is by far the most energy efficient way of ionizing a cold gas [1, 16, 17, 18, 19, 20, 22, 25, 29]. However, the practical feasibility of using an elec-

tron beam as an ionizer has yet to be demonstrated. It has proven to be a complex technical problem that is far from implementation [25].

Despite the lack of feasible technology to test these theories about MGD flow control, research has been underway using CFD codes [1, 7, 16, 17, 18, 19, 20, 23, 24, 29]. This allows researchers to see detailed flow paths, complex parameter interactions, and determine what kinds of forces and energies are required to make MGD flow control a reality. At the heart of scramjet research and design is a need to know, understand, and control the complex flow paths through the engine. CFD has played a major role in visualizing and understanding flow paths and creating a broad foundation of data on which to base new designs. In many cases CFD visualizes flows that are too complex to capture in flight test, or simply impossible to replicate due to lack of technology. MGD flow control is one example of a concept that is expensive and very difficult, if not impossible, to demonstrate in anything but a computational domain. Still, the data collected from computational simulations can be used in future applications when technology has caught up with the designs of today's engineers.

A. Kuranov and E. Sheikin at the Hypersonic Systems Research Institute in St. Petersburg, Russia developed the "AJAX" concept using such a numerical approach. The "AJAX" concept was one of the first designs to incorporate energy management as a fundamental design parameter [1, 16, 17, 18, 19, 20]. The Magneto-Plasma-Chemical Engine (MPCE), also referred to as a scramjet with MGD bypass, was developed within the framework of the AJAX concept and serves as the model for their MGD experiments. The engine shown in Figure 1.2 is a simplified scheme for the MGD bypass scramjet. It is comprised of five sections, including the inlet, MGD generator, combustor, MGD accelerator, and nozzle. The inlet in section 1 uses the underbody of the aircraft as the compression ramp and also includes an ionizer to give the flow the proper conductivity to interact with the forces in the MGD generator and accelerator. As mentioned before, standard air will not sufficiently ionize at the flight

conditions a scramjet will encounter, and the application of external power sources to ionize the flow is required. This is called non-equilibrium ionization [18, 22]. Kuranov and Sheikin have used the electron beam as the optimal ionizer based on minimization of the power spent to ionize the flow [18].

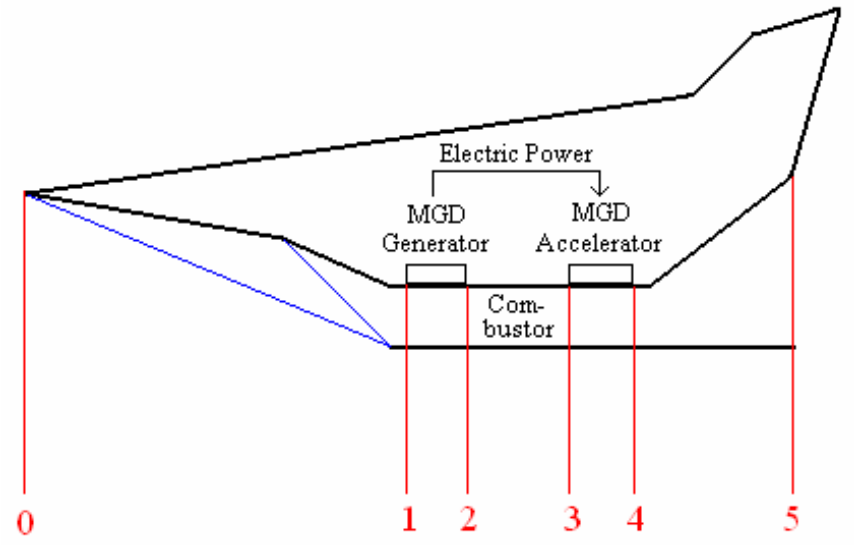

Figure 1.2 Simplified Magneto-Plasma-Chemical Engine (MPCE) [19].

The MGD generator serves several purposes. The forces in the generator are oriented such that a retarding Lorentz force is tangent and in the opposite direction to the flow. This is used to reduce or eliminate Mach reflection by extracting energy from the flow itself. This helps to sustain supersonic combustion and minimizes the chances of engine unstart. The MGD accelerator is designed such that the Lorentz force vector is oriented in the same direction as the flow, creating an accelerating Lorentz force. By introducing energy back into the flow, the thrust and specific impulse increase, thus improving the overall efficiency of the scramjet.

The AJAX concept is the first design to place a large focus on energy management. The electric power produced by the MGD generators is spent by the ionizer and onboard systems and for additional acceleration of combustion products in the MGD accelerator [1, 16, 17, 20]. The MPCE is designed to be used in a

self-sustained operational mode, which means that the electric power produced by the MGD generator exceeds the electric power necessary for both flow ionization and MGD acceleration [17]. This requirement drives the design to minimize power used in flow ionization and to maximize the power produced by the MGD generators.

The majority of Kuranov and Sheikin's research done with the AJAX concept has been using quasi 1-D and 2-D approaches, and conclusions seem to be promising. In early research, the MPCE showed that off-design flow conditions produced the greatest positive effect of MGD methods for flow control [16, 17]. Extending upon this, Kuranov and Sheikin broke down the influence of MGD further, concluding the extent of MGD influence on scramjet performance essentially depends on the type of MGD generator, inlet characteristics, load factors, Hall parameter, ionizer parameters, and flow parameters. The problem then becomes finding the optimal type and choice for these parameters to improve specific impulse and thrust given a specific flight condition [20].

In their most resent work, Kuranov and Sheikin explained the reason for enhanced performance: Decreasing the total pressure losses in the scramjet combustor using MGD bypass is the main reason for improved performance [19]. Furthermore, they assert that variation in specific impulse due to MGD bypass depends upon the nozzle configuration. These results agree with the conclusions of other researchers in that MGD holds significant promise for lowering the flow temperature and velocity in the combustor and extending the effective operating range of hypersonic air-breathing engines [2, 19, 21, 22, 25, 28].

1.3 Current Research

This research effort is a part of the ongoing study related to MGD flow control inside a scramjet engine. The goal is to determine the conditions required for a self-sustained mode of operation in which the power required to ionize the flow and the power required by the accelerator to enhance the thrust do not exceed the power

produced by the MGD generator. This parametric study is focused specifically on the development of the MGD accelerator and determining under what conditions the accelerator is most effective at controlling the flow.

Gaitonde's work has focused on a simplified scramjet engine shown in Figure 1.3 [7]. The present research is a continuation of his work, with a focus on the MGD accelerator. The MGD accelerator, with 4° diverging wall angles for all but the lower surface, serves to expand the flow. The nozzle side and bottom surfaces terminate where the width of the configuration equals that at the entrance: this facilitates the possibility of ganging such engines in a side-by-side fashion. The last component, the thrust surface, corresponds to an assumed underside of the vehicle of sufficient length to ensure that the flow is over-expanded at the exit of the computational domain. The MGD accelerator in the nozzle consists of segmented electrodes to supply the transverse electric current. The accelerator also has a magnetic field perpendicular to the electric current such that the Lorentz force accelerates the flow. The same MGD accelerator geometry used by Gaitonde is employed in the present research, however continuous electrodes are used to provide the electric field.

Gaitonde concluded that despite non-uniformities such as vortical structures and local flow reversals, overall generator operation is relatively efficient and can reduce the flow total temperature[7]. Furthermore, accelerator operation was shown to be less efficient with significant Joule heating effects in the boundary layer.

The goal of this preliminary computational study is to determine what effect specific conditions have on MGD accelerator operation in a realistic scramjet nozzle. In particular, the parameters of electric field strength, conductivity, and viscous effects will be addressed. The effect of these parameters on scramjet performance will be discussed in terms of specific thrust improvements.

This numerical study employs a 3-D MGD Computational Fluid Dynamics code [6, 7, 8, 9, 10, 11]. The code was written by the Computational Sciences Branch of the Aeromechanics Division of the Air Vehicles Directorate (VAAC) within

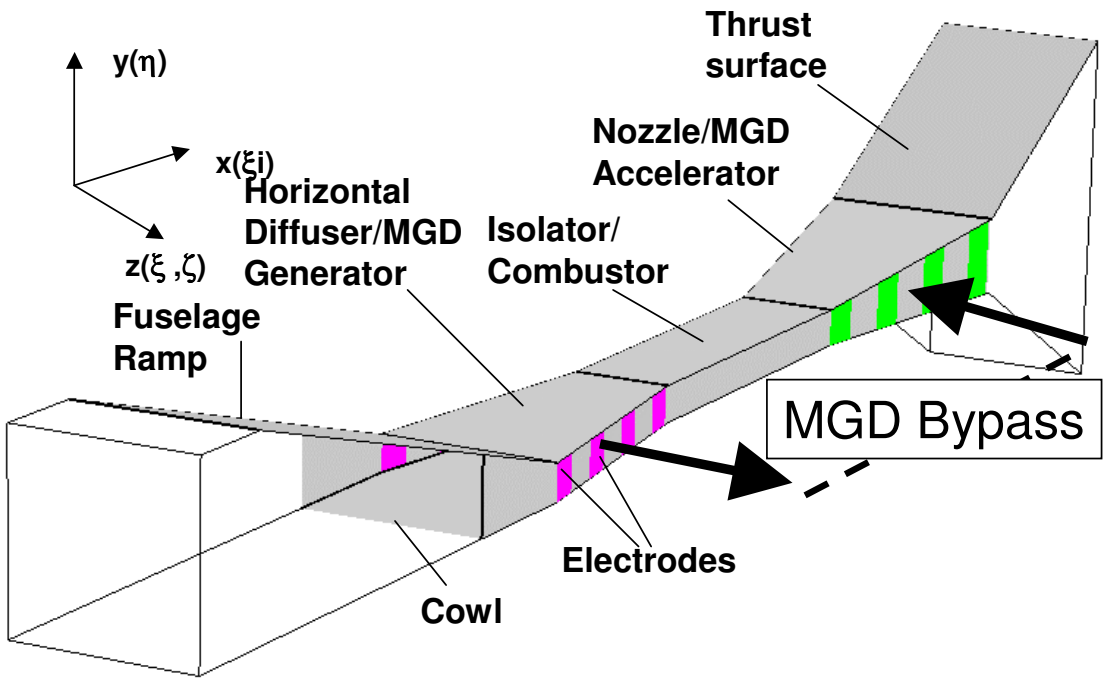

Figure 1.3 Simplified Mach 8 scramjet model design[7].

the Air Force Research Laboratory (AFRL). The code solves the Euler or Navier-Stokes equations with the addition of source terms for the MGD forces and energy interactions. The AFRL/VAAC code has been verified for various problems including 2-D flow past a flat plate and a laminar MGD boundary layer flow[8, 10].

The MGD governing equations used in this research are developed in Section 2 from the Navier-Stokes equations and the Maxwell equations. In section 3, the numerical algorithms used to solve the magnetogasdynamic equations are explained. Section 3 also includes a detailed explanation of the the computational domain set-up for this research. Section 4 presents the results of the baseline models without MGD interaction and includes MGD results for varying electric field strength and conductivity patterns. Of primary interest is the increase in thrust produced by MGD interactions over the non-MGD solutions. Section 5 presents some conclusions on the effect these parameters have on flow acceleration.

2. Governing Equations

2.0.1 The Vector Form Navier-Stokes Equations. The Navier-Stokes equations, based upon conservation of mass, momentum, and energy, are the governing equations of fluid flow. When heat transfer and body forces are neglected, the Navier-Stokes equations can be written in conservative vector form as shown [13]:

$$\frac{\partial U}{\partial t} + \frac{\partial \mathbf{E}}{\partial x} + \frac{\partial \mathbf{F}}{\partial y} + \frac{\partial \mathbf{G}}{\partial z} = S \tag{2.1}$$

U is the vector of conservative variables given by:

$$U = [\rho \quad \rho u \quad \rho v \quad \rho w \quad \rho e_t]^T \tag{2.2}$$

E, **F**, and **G** represent the total fluxes in the x, y, and z directions respectively. These fluxes can be broken down into inviscid and viscous vector terms as shown:

$$\mathbf{E} = E_i - E_v = \begin{bmatrix} \rho u \\ \rho u^2 + p \\ \rho u v \\ \rho u w \\ \rho h_t u \end{bmatrix} - \begin{bmatrix} 0 \\ \tau_{xx} \\ \tau_{xy} \\ \tau_{xz} \\ u\tau_{xx} + v\tau_{xy} + w\tau_{xz} + q_x \end{bmatrix} \tag{2.3}$$

$$\mathbf{F} = F_i - F_v = \begin{bmatrix} \rho v \\ \rho u v \\ \rho v^2 + p \\ \rho v w \\ \rho h_t v \end{bmatrix} - \begin{bmatrix} 0 \\ \tau_{xy} \\ \tau_{yy} \\ \tau_{yz} \\ u\tau_{xy} + v\tau_{yy} + w\tau_{yz} + q_y \end{bmatrix} \tag{2.4}$$

$$\mathbf{G} = G_i - G_v = \begin{bmatrix} \rho w \\ \rho u w \\ \rho v w \\ \rho w^2 + p \\ \rho h_t w \end{bmatrix} - \begin{bmatrix} 0 \\ \tau_{xz} \\ \tau_{yz} \\ \tau_{zz} \\ u\tau_{xz} + v\tau_{yz} + w\tau_{zz} + q_z \end{bmatrix} \tag{2.5}$$

Lastly, S is the source term defined without MGD as:

$$\mathbf{S} = \begin{bmatrix} 0 \\ 0 \\ 0 \\ 0 \\ 0 \end{bmatrix} \tag{2.6}$$

2.0.2 Ideal Gas Law. As shown above, the vector equations have six variables, (ρ, u, v, w, p, e_t), but only 5 equations. The ideal gas law provides the sixth equation to close the system. With the assumption that air is a calorically perfect gas, and using $\mathcal{R}$ as the universal gas constant for air, the ideal gas law is given as:

$$p = \rho \mathcal{R} T \tag{2.7}$$

2.1 Maxwell Equations

Maxwell's equations are the governing equations of electromagnetics, comprised of laws from Coulomb, Gauss, Faraday, and Ampere [14]. An important discussion when dealing with Maxwell's equations is the principle of special relativity. The coupling of electromagnetic, fluid-dynamic, and thermodynamic forces results from a conducting media in motion. Measured values of these physical properties are taken in the laboratory frame, where the media is moving relative to the

observer. A second frame of reference is also taken into consideration, the 'rest frame' where the observer is at rest compared to the media. Electromagnetic field quantities are related from one frame to the other using the Maxwell-Lorentz transformations. The Maxwell equations are valid in all reference frames, including the laboratory and the rest frame (denoted by a prime), and are given as:

$$\nabla \cdot \vec{E} = \frac{\rho_e}{\epsilon_e} \tag{2.8}$$

$$\nabla \cdot \vec{B} = 0 \tag{2.9}$$

$$\nabla \times \vec{E} = -\frac{\partial \vec{B}}{\partial t} \tag{2.10}$$

$$\nabla \times \vec{B} = \mu_e \vec{j} + \mu_e \epsilon_e \frac{\partial \vec{E}}{\partial t} \tag{2.11}$$

where $\vec{E}$ is the electric field, $\vec{B}$ is the magnetic flux density, $\vec{j}$ is the conduction current density, μ_e is the permeability, and ϵ_e is the permittivity.

2.1.1 Ohm's Law. Ohm's law is defined for linear isotropic media in the rest frame as follows:

$$j_i' = \sigma E_i' \tag{2.12}$$

where σ is the conductivity.

As mentioned, the Maxwell-Lorentz transformations are used to transform the Maxwell equations from the rest frame to the laboratory frame. When the media is nonuniform in all directions, anisotropic, and $V^2 << \mathbf{c}^2$, generalized Ohm's law is as follows[14]:

$$j_i = \sigma_{ji}[E_j + (\vec{V} \times \vec{B})_j] + \rho_e V_i \tag{2.13}$$

2.1.2 Constitutive Relations. The constitutive relations for linear isotropic dielectrics and magnetic materials expressed in the laboratory frame are as follows when $V^2 << \mathbf{c}^2$ and the medium is isotropic [14]:

$$\vec{D} = \epsilon_e[\vec{E} + (1 - \frac{1}{\frac{\epsilon_e}{\epsilon_{0,e}}\frac{\mu_e}{\mu_{0,e}}})\vec{V} \times \vec{B}] \tag{2.14}$$

$$\vec{B} = \mu_e[\vec{H} - (1 - \frac{1}{\frac{\epsilon_e}{\epsilon_{0,e}}\frac{\mu_e}{\mu_{0,e}}})\vec{V} \times \vec{D}] \tag{2.15}$$

2.1.3 Magnetogasdynamic Assumptions. When a conductive fluid moves through a magnetic field, there is an interaction between the fluid and electromagnetic field. This interaction is called plasma dynamics and has been studied for over 100 years. When this is applied to a fluid continuum, it is called magnetofluid-mechanics (MFM). The equations used to describe the interactions between a fluid media and electromagnetic fields are based upon a set of assumptions. When these equations are applied to air as the fluid media, the MGD equations emerge as a subset of the MFM equations. The MGD assumptions are as follows [14]:

MGD Assumption 1: $|V|^2 << \mathbf{c}^2$, the magnitude of the velocities dealt with in fluid dynamics are much less than the speed of light.

MGD Assumption 2: $\vec{E} \approx \mathcal{O}(\vec{V} \times \vec{B})$ implies that the induced magnetic field is much smaller than the externally applied magnetic field.

MGD Assumption 3: $\frac{\partial \vec{D}}{\partial t} \approx 0$, disregarding phenomena due to high frequency and $\frac{\partial \vec{E}}{\partial t} \approx 0$ by the constitutive relations. Therefore, $\nabla \times \vec{B} = \mu_e \vec{j}$.

MGD Assumption 4: The electric energy is insignificant compared to the magnetic energy.

MGD Assumption 5: The conductivity is considered independent of magnetic field. This assumption implies that $\vec{j}' = \vec{j}$.

MGD Assumption 6: Force density is represented by $\vec{f} = \rho_e \vec{E} + \vec{j} \times \vec{B}$.

2.1.4 Maxwell Equations for Magnetogasdynamic Flow. When the assumptions listed above are included in the Maxwell Equations, they yields a new set which govern electromagnetic fields. In the laboratory frame they become[14]:

$$\nabla \times \vec{E} = -\frac{\partial \vec{B}}{\partial t} \tag{2.16}$$

$$\nabla \times \vec{B} = \mu_e \vec{j} \tag{2.17}$$

$$\nabla \cdot \vec{j} = 0 \tag{2.18}$$

$$\nabla \cdot \vec{B} = 0 \tag{2.19}$$

And, Ohm's law becomes:

$$\vec{j} = \sigma(\vec{E} + \vec{V} \times \vec{B}) \tag{2.20}$$

All subsequent equations are written in the laboratory frame unless otherwise noted.

2.2 Magnetogasdynamic Equations

The magnetogasdynamic equations are the combination of the Maxwell equations for MGD and the Navier-Stokes equations from the beginning of this chapter. These equations describe the interaction between electromagnetic fields and electrically conducting gases in a continuum governed by the MGD assumptions. The magnetogasdynamic equations are the same as those given in Eqns. 2.1 except the term S is now given by:

$$\mathbf{S} = \begin{bmatrix} 0 \\ j_y B_z - j_z B_y \\ j_z B_x - j_x B_z \\ j_x B_y - j_y B_x \\ E_x j_x + E_y j_y + E_z j_z \end{bmatrix} \tag{2.21}$$

where $(\vec{j} \times \vec{B})$ components are the Lorentz force components, and the $\vec{E} \cdot \vec{j}$ term is the resulting energy interaction.

2.2.1 Non-dimensionalizing the Magnetogasdynamic Equations. The MGD equations are non-dimensionalized as follows where the dimensionless quantities are denoted by an asterisk [14]:

$$\begin{aligned} L^* &= \frac{L}{L_0} & \vec{V}^* &= \frac{\vec{V}}{V_0} \\ \rho^* &= \frac{\rho}{\rho_0} & T^* &= \frac{T}{T_0} \\ \vec{E}^* &= \frac{\vec{E}}{E_0} & \vec{B}^* &= \frac{\vec{B}}{B_0} \end{aligned} \tag{2.22}$$

These initial dimensional quantities denoted by 0 are used to non-dimensionalize the other variables, and all dimensionless variables are substituted into the equations. Several non-dimensional parameters are formed during this process which help to characterize MGD flows. The Reynolds number is the ratio of inertial forces to viscous forces, defined as follows:

$$Re = \frac{V_0 L_0}{\nu_f} \tag{2.23}$$

The magnetic Reynolds number is a measure of the magnitude of the induced magnetic field compared to the total magnetic field:

$$Rm = V_0 L_0 \sigma_0 \mu_{0,e} \tag{2.24}$$

The Mach number and magnetic Mach number are defined as follows:

$$M = \frac{V_0}{a_0} \tag{2.25}$$

$$M_m = \frac{V_0\sqrt{\rho_0\mu_{0,e}}}{B_0} \tag{2.26}$$

The Prandtl number is the ratio of kinematic viscosity to thermal diffusivity:

$$Pr = \frac{c_P\nu_f\rho_0}{\kappa_f} \tag{2.27}$$

The magnetic Prandtl number is the ratio of vorticity diffusion to magnetic diffusion:

$$Pm = \sigma_0\nu_f\mu_{0,e} = \frac{Rm}{Re} \tag{2.28}$$

The interaction parameter, $\mathcal{Q}$, is used when $Rm << 1$ and is defined as the ratio of the ponderomotive force to the inertial force and should be $\mathcal{O}(1)$. By increasing $\mathcal{Q}$ the magnitude of the magnetic field is increased.

$$\mathcal{Q} = \frac{\sigma_0 B_0^2 L_0}{\rho_0 V_0} = \frac{Rm}{M_m^2} \tag{2.29}$$

The load factor, $\mathcal{K}$, is defined as the ratio of the electric field to the induced effects. An increase in $\mathcal{K}$ signifies a larger applied electric field, E_0.

$$\mathcal{K} = \frac{-E_0}{B_0 V_0} \tag{2.30}$$

In the MGD source terms, the non-dimensional Lorentz force is $\mathcal{Q}(\vec{j}^* \times \vec{B}^*)$ and the non-dimensional energy interaction is $\mathcal{Q}\vec{E}^* \cdot \vec{j}^*$.

3. Computational Set-Up

This section presents the computational code, domain, and factors employed in this parametric study on MGD acceleration.

3.1 MGD 3-D Computational Code

The computational study employed the 3-D non-dimensional MGD CFD code [6, 7, 8, 9, 10, 11]. The code was written by AFRL/VAAC. This code solves the Euler or Navier-Stokes equations with the addition of a source term to account for the MGD Lorentz forces and energy interaction.

The inviscid flux vectors for this generalized coordinate finite difference code were discretized using Roe's flux-difference splitting method with a van Leer harmonic limited Monotone Upstream-centered Schemes for Conservation Laws (MUSCL) variable extrapolation. The limited MUSCL variable extrapolation provided essentially third-order spatial accuracy throughout the smooth region of the flow. The viscous flux vectors were discretized using central differences.

Beam-Warming implicit time integration scheme was employed to integrate the MGD system of equations to steady state using a constant time step. In addition, a Gauss-Siedel Successive Overrelaxation method was applied to the current continuity Poisson equation to determine the electric field within the computational domain for MGD simulations.

3.2 Thrust Calculation Model

In order to assess how the thrust of the MGD accelerator changes as the parameters are varied, the stream thrust function is calculated at the inlet and exit of the accelerator/nozzle [12]. The stream thrust function is the parameter that leads to the determination of mass flow rate specific thrust, and is given as follows:

$$Sa = \frac{I}{\dot{m}} \tag{3.1}$$

where I is the axial impulse function given as:

$$I = pA(1 + \gamma M^2) \tag{3.2}$$

I measures the axial force imposed on the flow between two axial stations, in this case the MGD accelerator inlet and exit. These equations are based upon the following set of assumptions [12]:

Sa **Assumption 1:** The flow is steady or the unsteady terms are negligible.

Sa **Assumption 2:** The ratio of momentum flux to pressure forces is large.

Sa **Assumption 3:** Thermochemistry of the flow must be known.

Sa **Assumption 4:** The velocity at each stage is aligned with the thrust or axial direction and the through-flow area is perpendicular to that direction.

Assumption 1 becomes valid in hypersonic flows since the steady flow inertial terms are very large. In addition, the axial impulse function includes a ratio of momentum flux to pressure forces in the term γM^2. In hypersonic flows, the greatest part of the impulse function is due to momentum flux, satisfying assumption 2.

The force exerted on the flow in the axial direction can be obtained from the stream thrust function as shown:

$$\frac{F_x}{\dot{m}} = u_e(1 + \frac{\mathcal{R}T_e}{u_e^2}) - u_i(1 + \frac{\mathcal{R}T_i}{u_i^2}) = Sa_e - Sa_i \tag{3.3}$$

The value of $Sa_e - Sa_i$ will be used to assess the influence of MGD acceleration on the flow.

3.3 Computational Domain

Preliminary designs for this research were comprised of both the accelerator/nozzle and thrust surface regions of the scramjet design used by Gaitonde [7]. Using a similar geometry, a grid convergence study was done for viscous flow calculations. Two grids were built, a coarse mesh with a node size of 141 x 31 x 31 and also a fine mesh of the size 281 x 61 x 61, which increased the number of cells by a factor of 8, from $126,000$ to $1,008,000$. The three dimensional and side view of the two grids is shown in Figure 3.1. Wall boundary conditions were specified for all sides in both regions. The inlet was characterized by a pressure inlet condition and the outlet by an outflow condition.

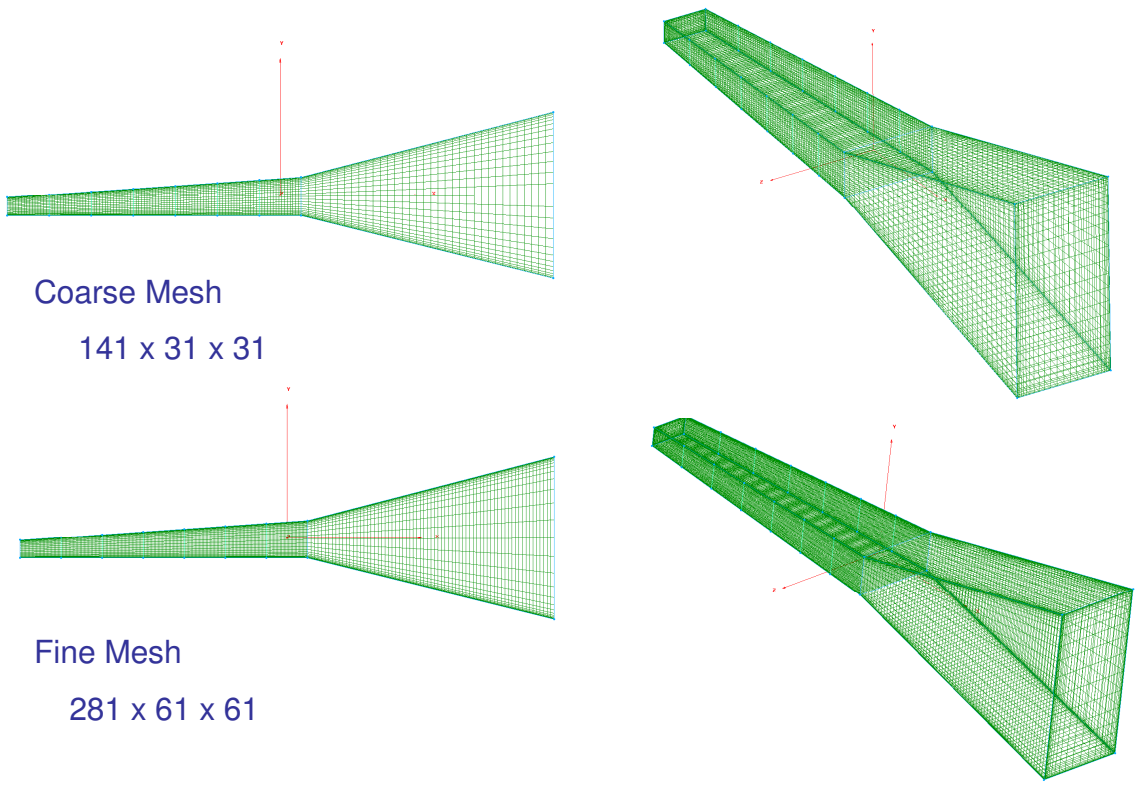

Figure 3.1 Preliminary design used in the grid convergence study.

Viscous solutions for both the fine and coarse mesh designs were obtained using Fluent v6.1.22. Convergence criteria was the same for both designs. A converged solution was reached by the coarse mesh in 102 iterations, over 100 less than the fine

mesh which took 220 iterations. Comparison of the solutions revealed that they were not significantly different. The resolution using the fine mesh was better, however the flow structures and point values in both solutions were virtually identical. As a result, the coarse mesh was chosen as the more efficient design.

In order to focus in on flow structures and the effect of MGD acceleration on the flow, the thrust surface aft of the accelerator was removed from the physical domain. This resulted in an accelerator region comprised of $95,400$ cells.

The dimensions of the MGD accelerator model are shown in Figure 3.2. These measurements are taken from the physical model used by Gaitonde [7]. The inlet area was 0.1075m^2 while the exit area was 0.4335m^2. The difference is due to a 4° divergence in the top and side walls while the bottom surface is held constant. This leads to an exit area to inlet area ratio of 4.032.

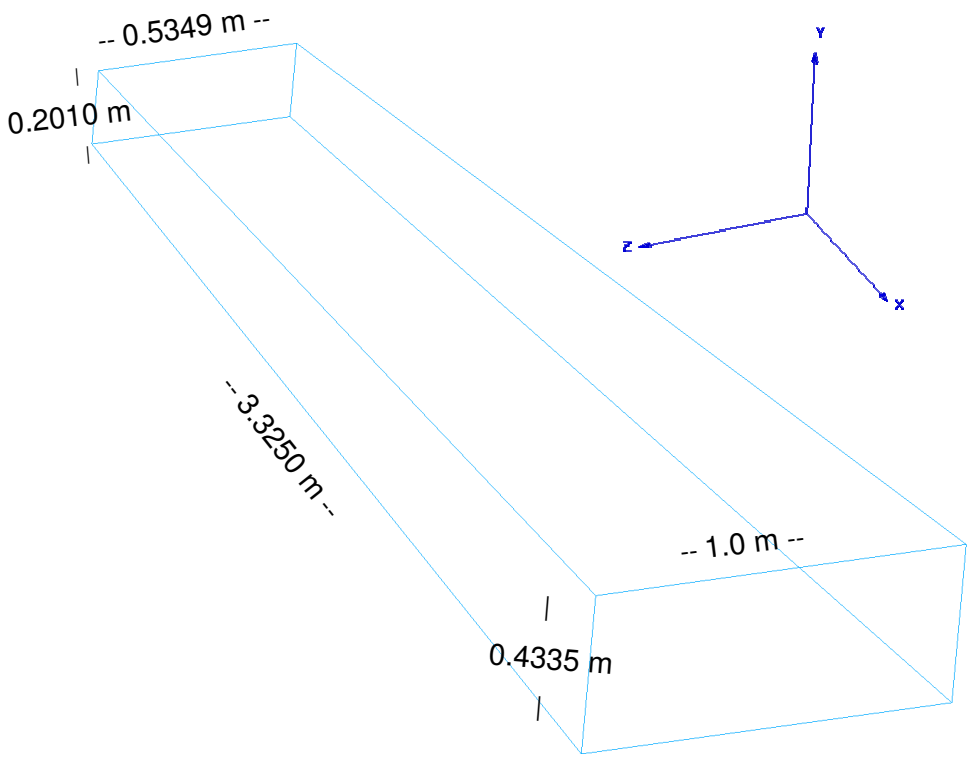

Figure 3.2 Three dimensional MGD accelerator geometry.

The inviscid and viscous grid designs used in this study were built using Gridgen v15. In anticipation of more complex flow structures using the MGD flow solver, additional nodes were added to the inviscid model. This resulted in a final mesh design with node dimensions of 120 x 41 x 51 yielding a numerical domain with $240,000$ cells which is shown in Figure 3.3. Equal spacing was specified in all three dimensions. In order to implement the inviscid boundary conditions, an orthogonal grid solver was used to force the grid lines perpendicular to the four MGD accelerator walls.

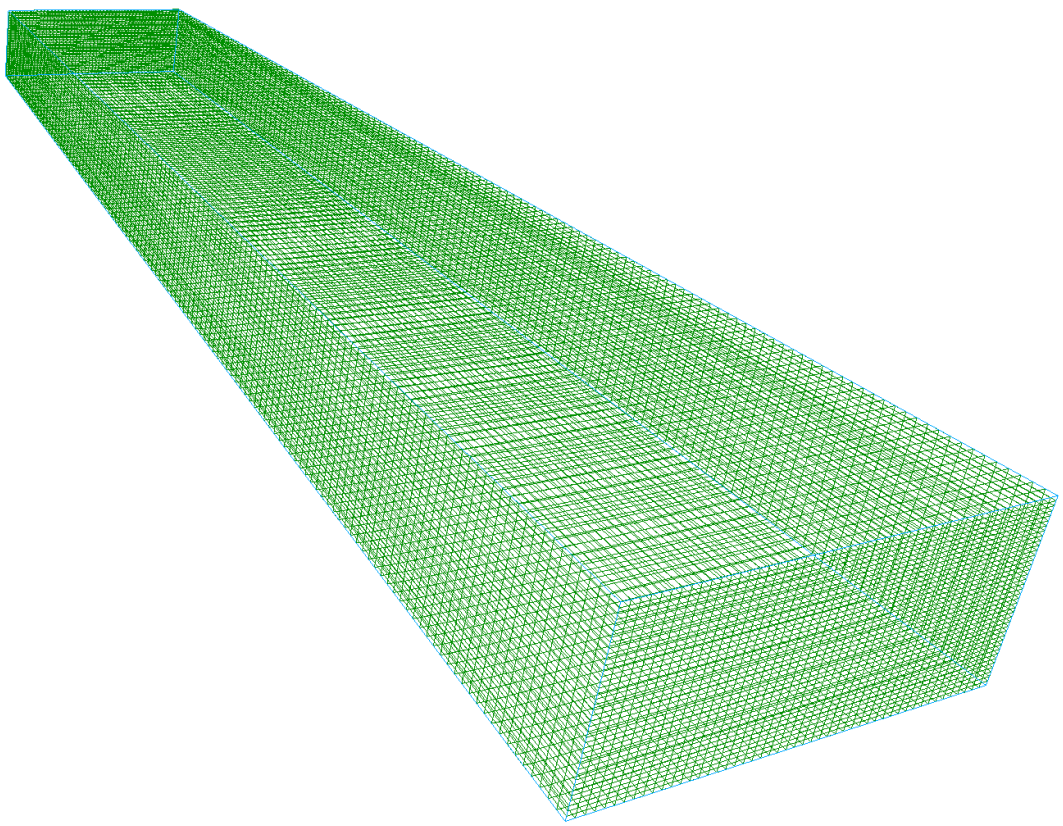

Figure 3.3 Three dimensional inviscid mesh design.

The number of points in the viscous grid was also increased from the convergence study in anticipation of flow complexity and to add extra cells in the boundary layer. The viscous grid had 10 cells in the boundary layer which was determined to be 5.38mm from laminar boundary layer theory. Again an orthogonal grid solver

in Gridgen was used to bring the mesh lines perpendicular at the walls. The final viscous grid shown in Figure 3.4 had 120 x 46 x 56 nodes and $297,000$ cells.

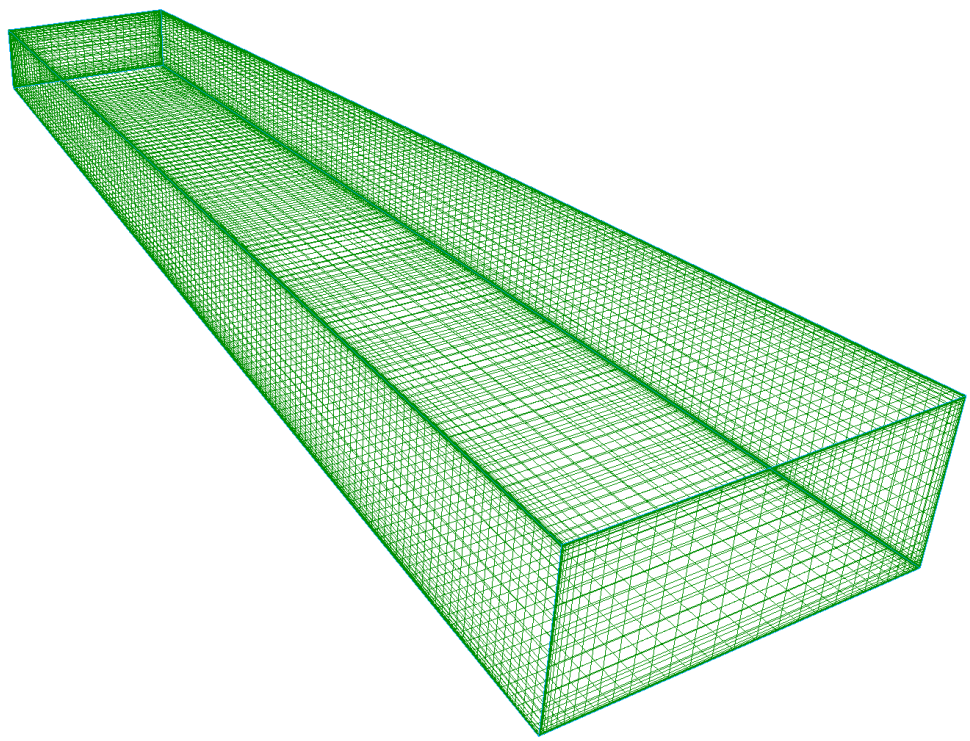

Figure 3.4 Three dimensional viscous mesh design.

3.4 Computational Parameters

The flow conditions used at the accelerator inlet were set using the Mach 8 design flight conditions employed by Gaitonde [7]. Table 3.1 shows the inlet conditions used in the numerical calculations. Also included in Table 3.1 are the free-stream values which were used in non-dimensionalizing the flow parameters.

One important parameter in MGD solutions is the flow conductivity pattern. To explore what effect conductivity, σ, has on flow acceleration, this study focused on two different patterns of σ. In both patterns, σ is a non-dimensional value based on a modified Gaussian distribution. The dimensional values of σ are related to the magnetic flux density, B_0, which may vary nominally from 2 tesla to 10 tesla for these applications. The non-dimensional values of σ_0 given this range are determined using

Table 3.1 Freestream and MGD Accelerator Inlet Conditions.

	Free-stream Conditions	Inlet Conditions	Non-Dimensional Inlet Conditions
Velocity	2380.45 m/s	1938.2 m/s	0.8142
Temperature	250° K	2892.0^o K	11.568
Pressure	1285.76 Pa	143116 Pa	1.4101
Mach	8	1.9148	1.9148

Eqn. 3.4 where the interaction parameter, $\mathcal{Q}$, is set to unity in this study. Eqn. 3.4 then becomes:

$$\sigma_0 = \frac{\rho_0 U_0}{B_0^2 L_0} \tag{3.4}$$

where $L_0 = 0.6$, and ρ_0 and V_0 are free-stream values from Table 3.1. This yields a range of σ_0 from 0.711 at a magnetic flux density of 10T to 17.778 at $2T$.

The first σ pattern is shown in Figure 3.5 where the mainstream accelerator flow region has high non-dimensional conductivity, or $\sigma = 1.0$, which falls off towards zero close to the walls. This configuration is designed to simulate electron beam type ionization, mentioned before as the most energy efficient means of ionization. The second configuration, shown in Figure 3.6, high conductivity is set close to the walls and σ is allowed to fall from 1.0 towards zero in the mainstream. This configuration is designed to simulate ionized particle seeding of the flow near the walls.

The second important parameter varied in this study was the load factor, $\mathcal{K}$, which was given in Eqn. 2.30. Recall that the magnetic flux density is non-dimensionalized by B_0 is unity for this investigation. This means that changes in the load factor cause changes in E_0, the magnitude of the applied electric field. Thus the load factor becomes a measure of the applied electric field intensity.

The Lorentz force given as $\vec{j} \times \vec{B}$ is applied to accelerate the flow in the MGD solution runs. The magnetic flux density, B_0, is oriented in the positive y direction. For the load factors used in this study, an electric current is produced in the negative

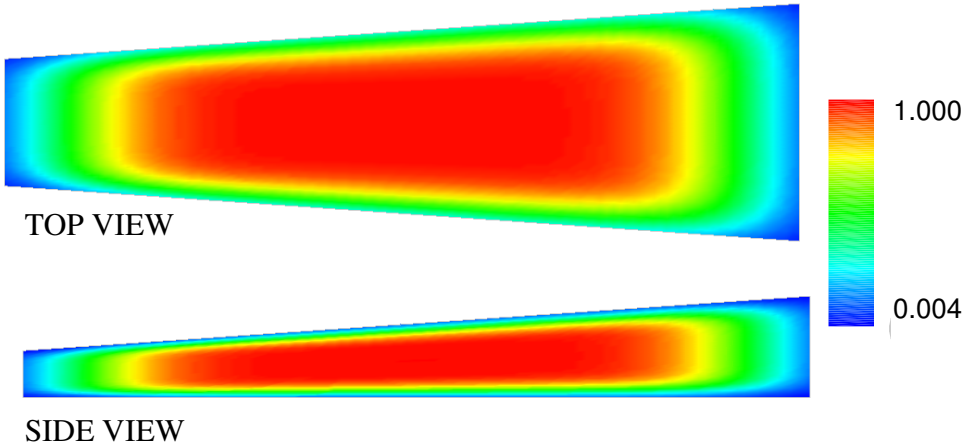

Figure 3.5 MGD accelerator conductivity pattern 1.

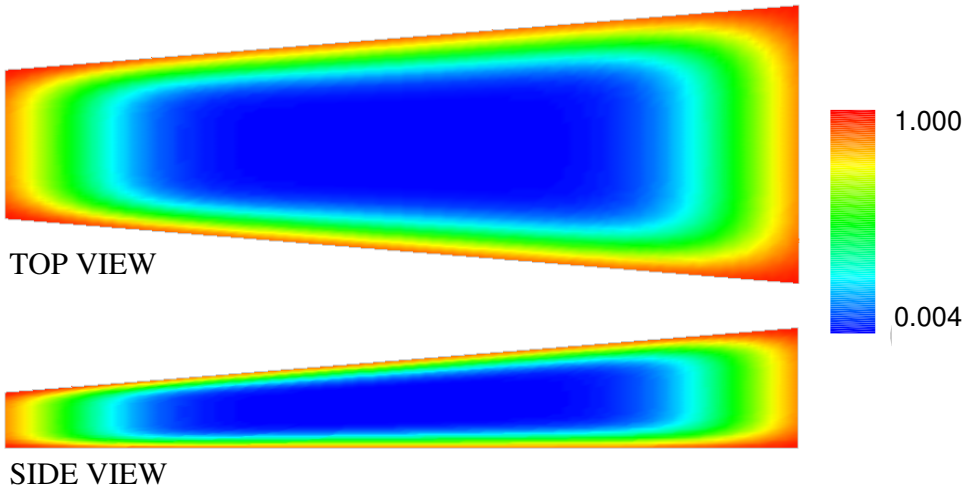

Figure 3.6 MGD accelerator conductivity pattern 2.

z direction which results in an accelerating Lorentz force in the positive x direction as shown in Figure 3.7.

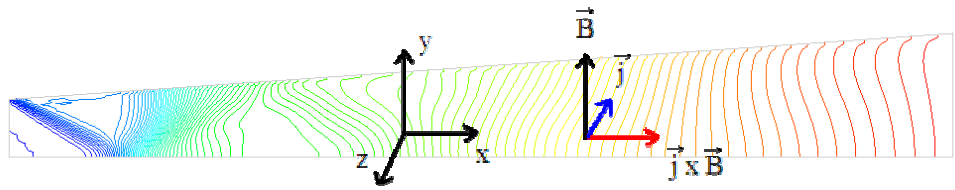

Figure 3.7 Schematic of an accelerating Lorentz force vector.

3.5 Computational Cases

The flow parameters of flow regime, conductivity, and electric field strength or load factor were varied in the course of eight test cases investigated. Case 1 and case 2 in this research were inviscid and viscous flow solution, respectively, with no MGD interactions. To establish baseline calculations for both the inviscid and viscous cases, the flows were initialized to the inlet conditions and iterated until the solutions converged. These converged solutions became the initial states for the subsequent MGD runs.

Inviscid MGD flow solutions were determined for several load factors and two conductivity patterns. Cases 3,4, and 5 represent inviscid solutions with load factors of 1.4, 1.2, and 1.8, respectively, all with conductivity pattern 1 shown in Figure 3.5. Case 6 is the numerical solution to an inviscid flow with a load factor of 1.4 in conductivity pattern 2 from Figure 3.6. Viscous MGD flow solutions were also determined for two load factors. Case 7 and 8 represent viscous flow solutions at load factors of 1.4 and 1.8, respectively. Table 3.2 summarizes the varying parameters for each test case presented in this study.

Table 3.2 Test Case Parameters.

Test Case	Flow Regime	Conductivity Pattern	Load Factor ($\mathcal{K}$)
1	Inviscid	none	none
2	Viscous	none	none
3	Inviscid	1	1.4
4	Inviscid	1	1.2
5	Inviscid	1	1.8
6	Viscous	1	1.4
7	Viscous	1	1.8
8	Inviscid	2	1.4

4. Results

The MGD accelerator described in Chapter 3 was used in this numerical study to investigate the influence of an accelerating lorentz force. A total of 8 test cases were conducted, 6 inviscid and 2 viscous, varying conductivity pattern and electric field strength. Table 3.2 shows the breakdown of these 8 cases according to the varying parameters. Non-MGD baseline cases were established and used as a reference in later MGD solutions. The objective was to determine if specific thrust was greater in MGD solutions than in the baseline solutions, and to investigate what impact MGD has on the flow field inside the accelerator.

4.1 Baseline Cases

The first stage of this investigation was to determine baseline solutions, inviscid and viscous flow fields, without MGD interactions. The solutions to these baseline numerical configurations were used to determine the effect MGD acceleration had on the flowfield and thrust calculations.

4.1.1 Case 1: Inviscid. The inviscid numerical solution for the accelerator/nozzle flow without MGD interactions provided the first baseline solution. For this case, the computational domain was initialized to the initial flow conditions at the inlet specified in Table 3.1. The converged solution for Mach number is shown in Figure 4.1. As expected, the flow accelerates as it expands through the accelerator reaching a maximum average Mach number of 3.07 at the MGD accelerator exit. The Mach number increases uniformly with slightly higher Mach in the lower corners approximately half way down the accelerator flow path as shown in Figure 4.1.

Pressure contours in Figure 4.2 further demonstrate the relatively smooth flow path through the accelerator. As expected, the pressure decreases from 131884Pa to 16787Pa along the length of the accelerator and exits while still 18 times the

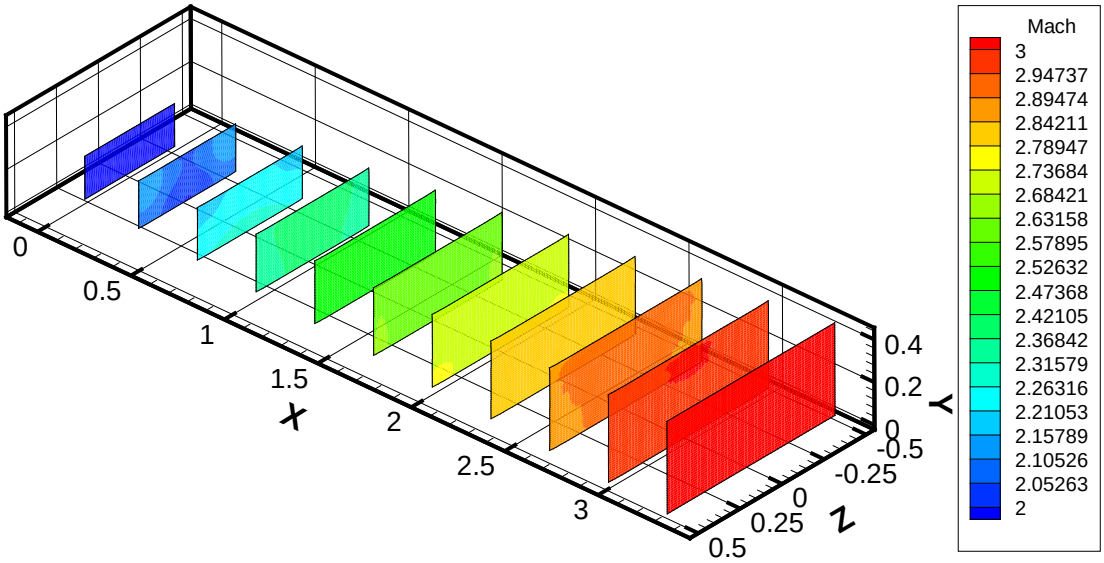

Figure 4.1 Case 1 - 3D inviscid results: Mach number.

free-stream pressure. Therefore, the flow is underexpanded. The flow structure at the accelerator inlet is due to the diverging walls on the sides and top, allowing the pressure to fall more rapidly than along the constant bottom surface.

Figure 4.3 shows the smooth temperature profile through the accelerator. As the flow expands along the walls on the top and sides, the temperature decreases faster than along the bottom surface, causing the area of high temperature on the bottom surface. The temperature values are with acceptable ranges according to the research, remaining below 3000K. The final parameter used to examine the flow is the velocity magnitude shown in Figure 4.4 ranging from 2,312 m/s at the accelerator inlet to 3,039 m/s at the exit. Like the two previous figures, the pressure contour plot shows a smooth flow through the accelerator.

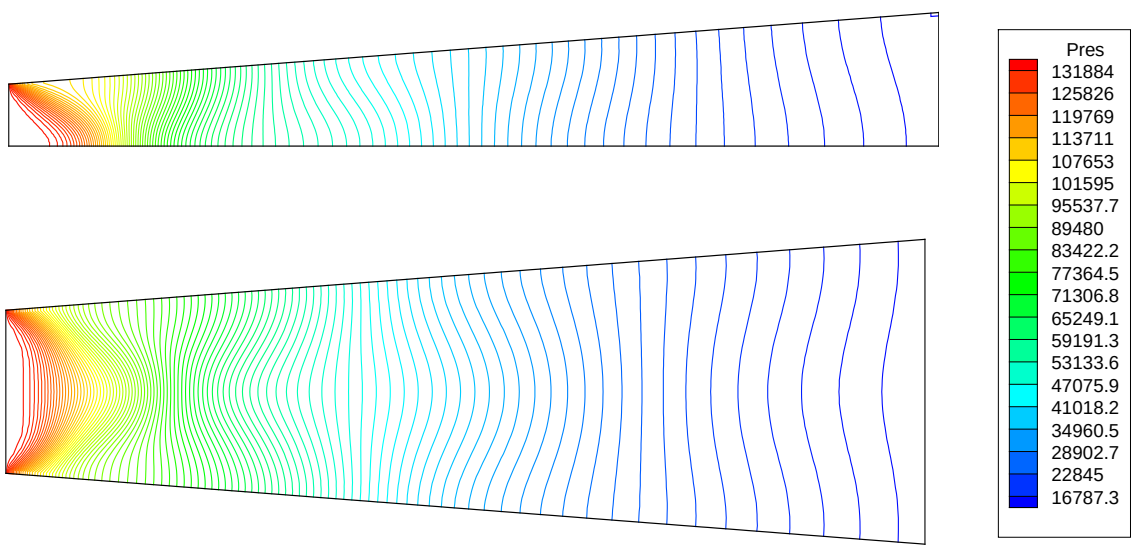

Figure 4.2 Case 1 - 2D inviscid contour lines: Pressure. (top: x-y midplane, bottom: x-z midplane)

4.1.2 Case 2: Viscous. A second baseline solution was determined for the viscous flow field through the accelerator/nozzle. As in Case 1, the computational domain was initialized to the initial flow conditions at the accelerator inlet. Figure 4.5 shows the Mach number as the flow expands through the accelerator. The majority of the flow field is unchanged from the inviscid solution in Figure 4.1 with

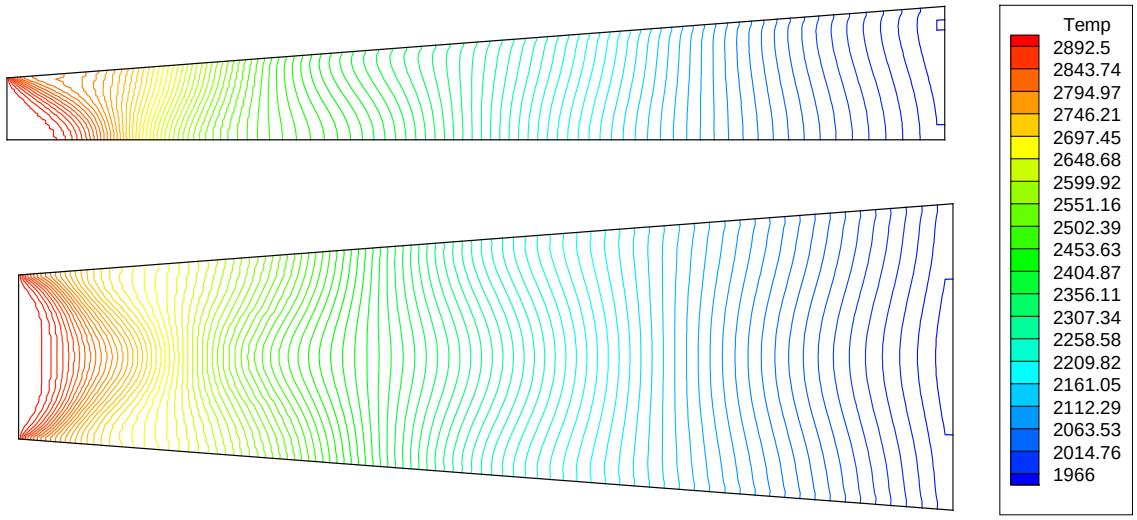

Figure 4.3 Case 1 - 2D inviscid contour lines: Temperature. (top: x-y midplane, bottom: x-z midplane)

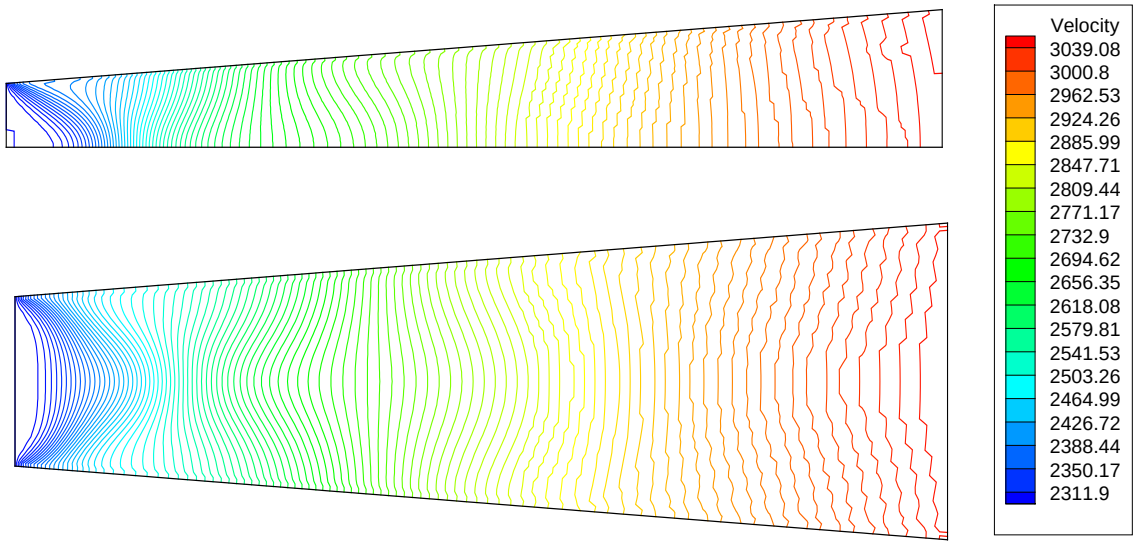

Figure 4.4 Case 1 - 2D inviscid contour lines: Velocity Magnitude. (top: x-y midplane, bottom: x-z midplane)

the exception of the boundary layer along the walls. For the viscous solution, the maximum average Mach number is 3.03 compared to 3.07 for the inviscid case. Figure 4.1 shows no significant flow structures besides the boundary layer developing in the flow field.

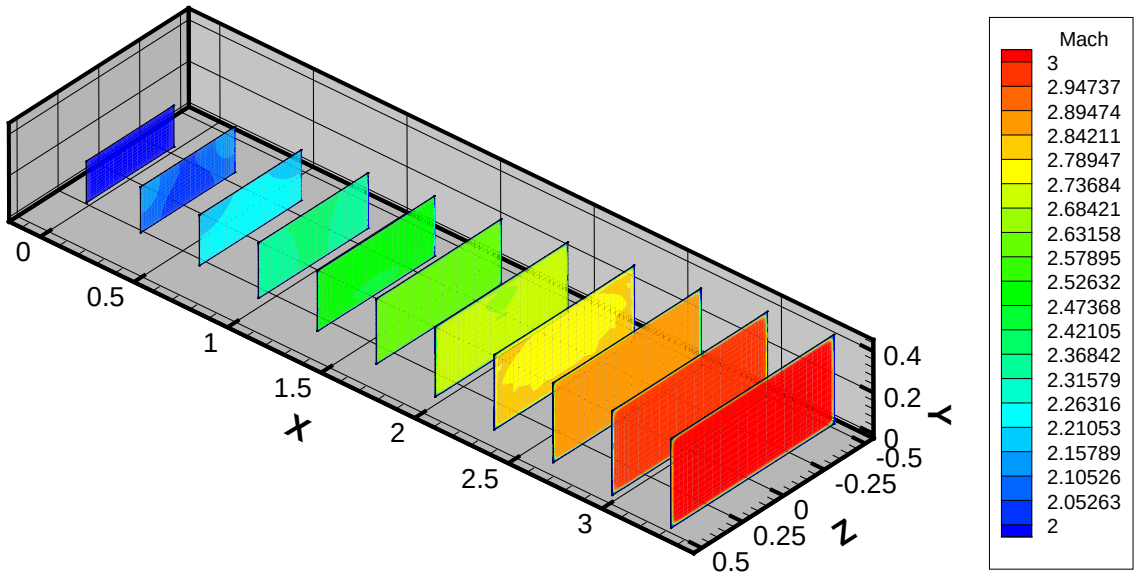

Figure 4.5 Case 2 - 3D viscous results: Mach number.

The pressure contours in Figure 4.6 again followed expected results, ranging from $135,199$Pa at the inlet to 17829Pa at the exit, slightly higher than the inviscid case. This is because viscous forces in the boundary layer reduce flow expansion. The temperature profile in Figure 4.7 is significantly different from the inviscid solution due to the viscous effects in the boundary layer. While the mainstream temperature ranges from approximately 2900K at the inlet to 2000K at the exit, the viscous effects in the boundary layer have heated the flow nearly 1000K. This 1000K increase is due to boundary layer heating and the use of an adiabatic boundary condition for the walls.

The laminar boundary layer profile shown in Figure 4.8 is along the bottom surface three cells from the accelerator exit where the boundary layer has fully developed. The vector lengths correspond to the velocity magnitude and colors to the

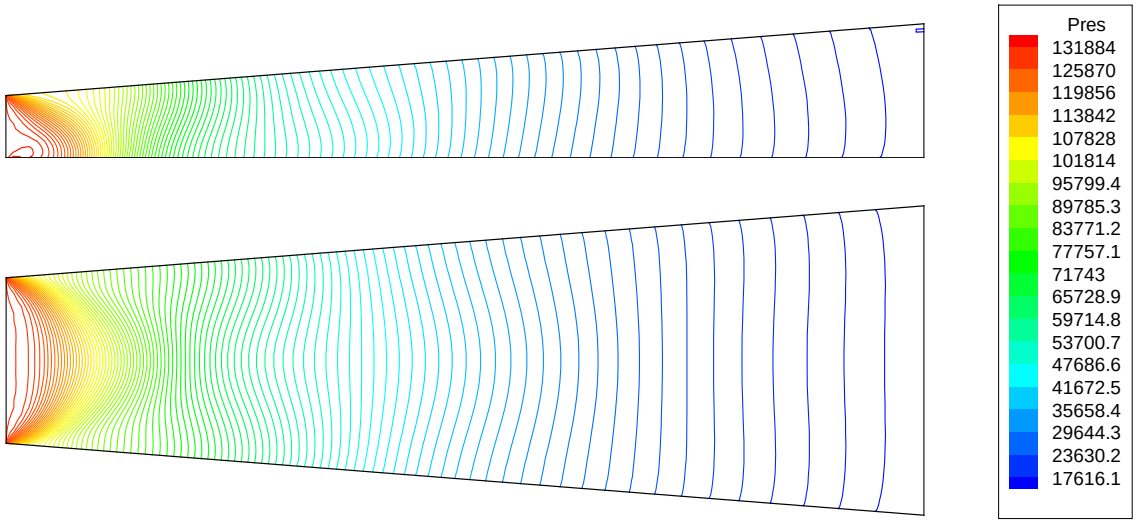

Figure 4.6 Case 2 - 2D viscous contour lines: Pressure. (top: x-y midplane, bottom: x-z midplane)

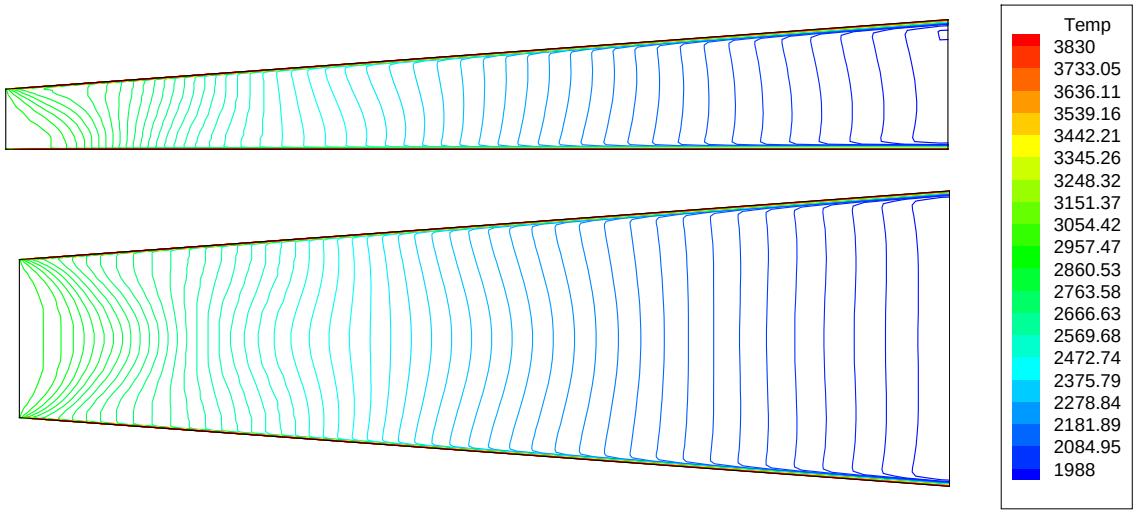

Figure 4.7 Case 2 - 2D viscous contour lines: Temperature. (top: x-y midplane, bottom: x-z midplane)

temperature at each point. As shown, the boundary layer extends out approximately 13 cells, or 1cm from the wall where the flow has reached mainstream velocity and temperature at this location.

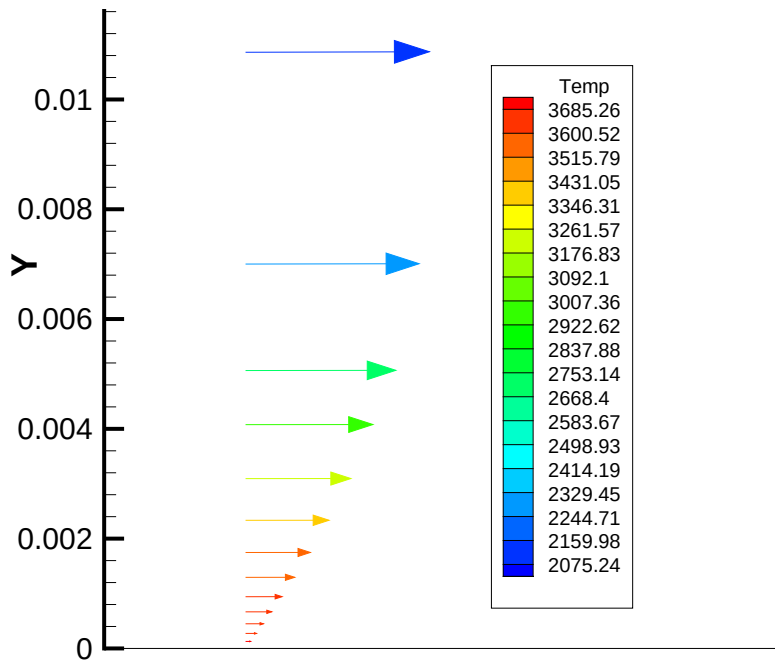

Figure 4.8 Case 2 - Viscous boundary layer profile.

4.2 MGD Results: Conductivity Pattern 1

The first set of the MGD solutions solved in this investigation used the conductivity pattern shown in Figure 3.5 known as conductivity pattern 1. This pattern simulates an electron beam ionization of the flow, non-dimensionally falling from unity in the mainstream towards zero at the walls, inlet, and exit. Three inviscid cases were solved using this conductivity pattern at load factors of 1.2, 1.4, and 1.8.

4.2.1 Case 3: Inviscid Load Factor 1.4. Case 3 of this investigation used a load factor, $\mathcal{K}$, of 1.4. The potential gradients between the two continuous electrodes on the side walls are established through the relation $\Delta\phi = \mathcal{K} w U_{ref} B$ where ϕ is the potential on the electrode, w is the width between the electrodes at the midway

point through the accelerator, and U_{ref} is a reference velocity at this midway point. In this study, B is set to unity. For $\mathcal{K} = 1.4$, the electrical potential is set to ± 0.5372 on the electrodes. The electric potential, ϕ, of the flow field for this load factor is shown in Figure 4.9. This contour plot shows the simulated electrodes along the span of each side wall creating the electric field. The electrode generating negative ϕ values is the anode, and the positive ϕ values are along the cathode.

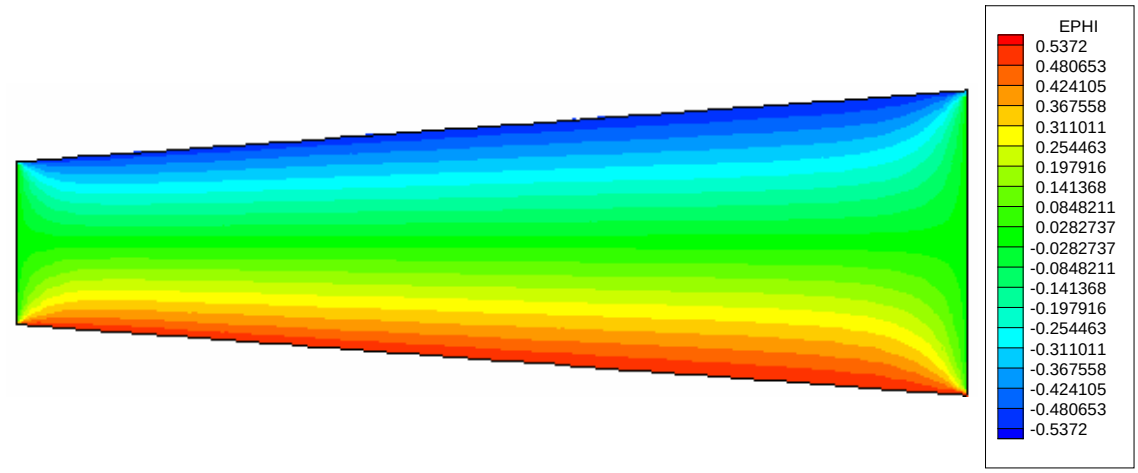

Figure 4.9 Case 3 - 2D electric field. (x-z midplane)

Due to the magnetic field oriented in the positive y direction, the load factor of 1.4 oriented the electric field in the negative z direction, which resulted in an accelerating Lorentz force. For this case, select Lorentz force vectors are shown in Figure 4.10. The vector plot shows the direction of the Lorentz force. When the force vectors are aligned with the flow in the positive x direction, the force is an accelerating Lorentz force, and when aligned in the negative x direction, a decelerating force. While most of the vectors are aligned in the x direction, the sides at the inlet and exit exhibit a different behavior. This is due to current 'leaking' around the edges of the electrodes, locally changing the orientation of the E field. The largest accelerating Lorentz force magnitude is in first half of the accelerator, from approximately 15% to 50% of the accelerator length. As shown in Figure 4.10, the vectors then decrease in magnitude and transition the force from an accelerating one

to a decelerating one. This transition occurs for Case 3 about 80% of the accelerator length. Beyond this transition, MGD begins decelerating the flow. This deceleration is expected since the reference velocity for determining the electric potential of the electrodes is taken at a location 50% of the accelerator length.

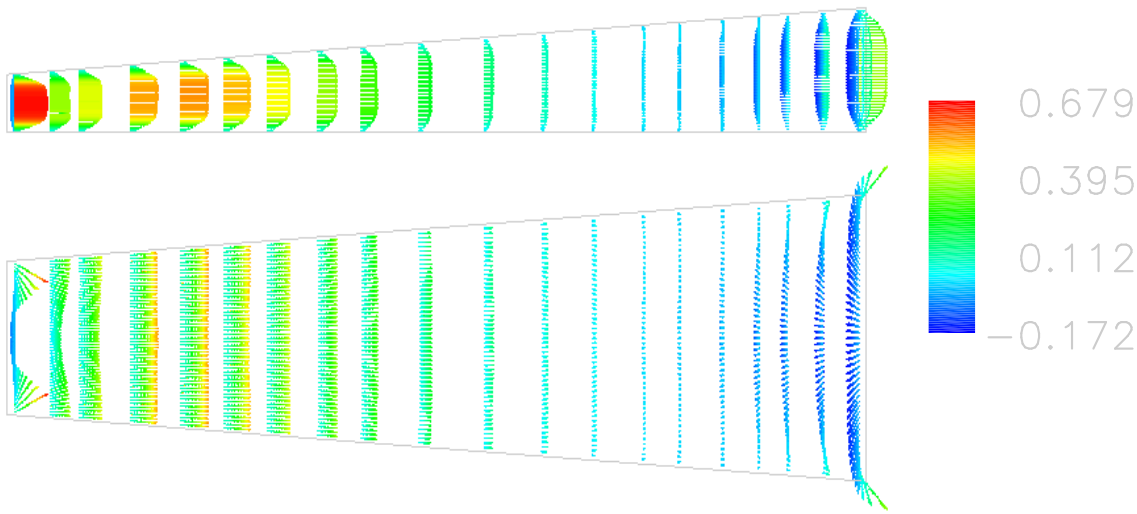

Figure 4.10 Case 3 - Lorentz vectors. (top: x-y midplane, bottom: x-z midplane)

Although the flow experiences both accelerating and decelerating Lorentz forces, MGD does have a significant impact on the flow field compared to non-MGD solutions. Figure 4.11 shows Mach number contours for this case. The maximum Mach number has increased 7.2% to 3.29. In addition, the location of largest Mach numbers is before the accelerator exit because the decelerating Lorentz force that develops near the exit works against the flow, slowing it down.

Another impact of MGD on the flow field is an increase in temperature along the walls and near the accelerator exit. Figure 4.12 shows the location of the highest temperatures along the electrodes and at the exit. The highest temperature for this case is 14.5% greater than the maximum temperature in Case 1. A closer look at the temperature contours in Figure 4.13 shows greater complexity in the flow field than was present in Case 1. The temperature gradients are much higher near the electrodes and in the corners of the accelerator. Along the electrodes as

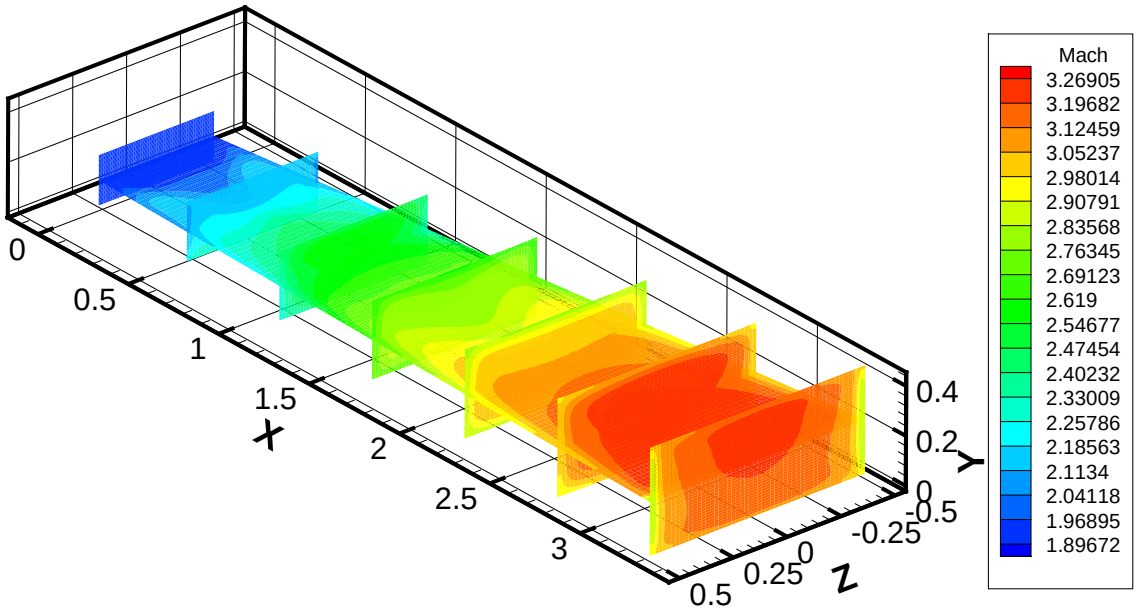

Figure 4.11 Case 3 - 3D inviscid results: Mach number.

shown in the x-z midplane view, the temperature is highest in the region of the accelerator corresponding to largest accelerating Lorentz force shown in Figure 4.10. The electrode surface side-plane view in Figure 4.13 shows that high temperatures fall off near the top and bottom edges of the electrode. The increase in temperature near the electrodes is due to the addition of energy into the flow through the energy interaction term. This energy interaction accounts for the Joule heating of the flow.

The pressure contours for this case are shown in Figure 4.14. The decelerating Lorentz force near the exit of the accelerator slows the expansion of the flow. The maximum pressure in the accelerator increased by 1.7% near the accelerator inlet.

Another implication of the accelerating and decelerating Lorentz forces is shown in the velocity contour plot in Figure 4.15. The flow exceeds the maximum velocity from Case 1 at approximately 50% of the accelerator length. In the transition region where the Lorentz force direction is switching, the flow velocity no longer increases, and near the exit the velocity decreases again.

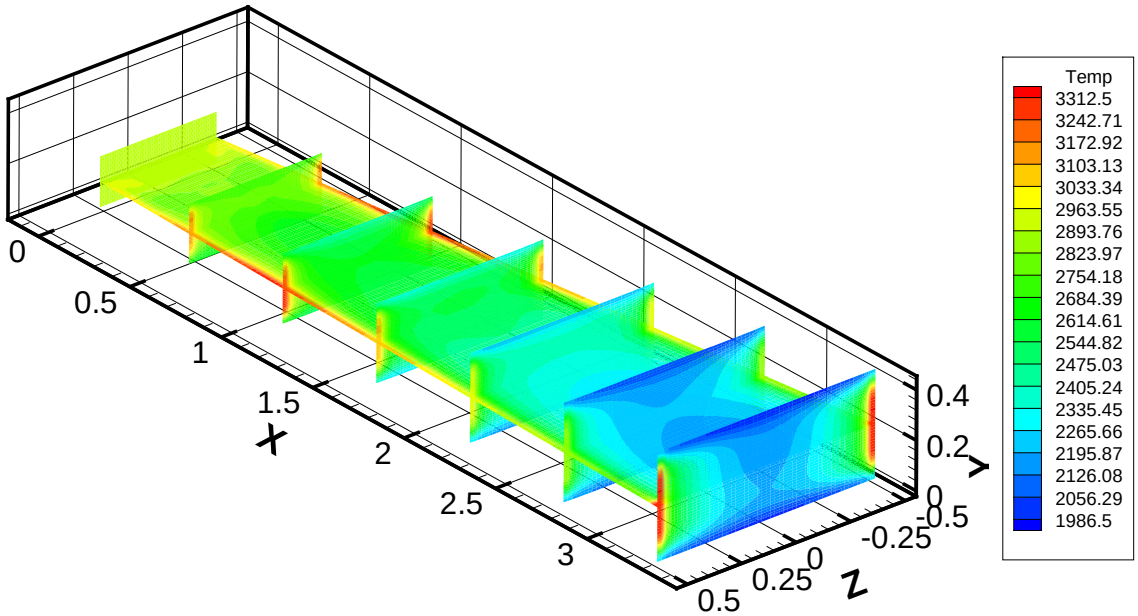

Figure 4.12 Case 3 - 3D inviscid results: Temperature.

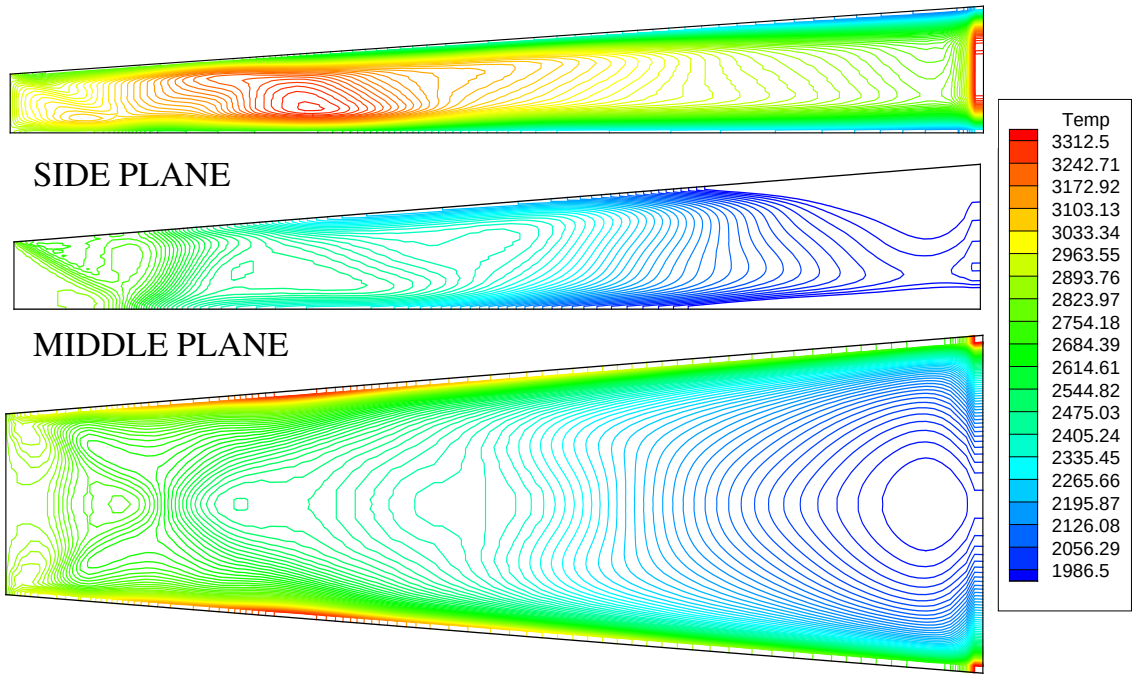

Figure 4.13 Case 3 - 2D inviscid contour lines: Temperature. (top: x-y side plane, middle: x-y midplane, bottom: x-z midplane)

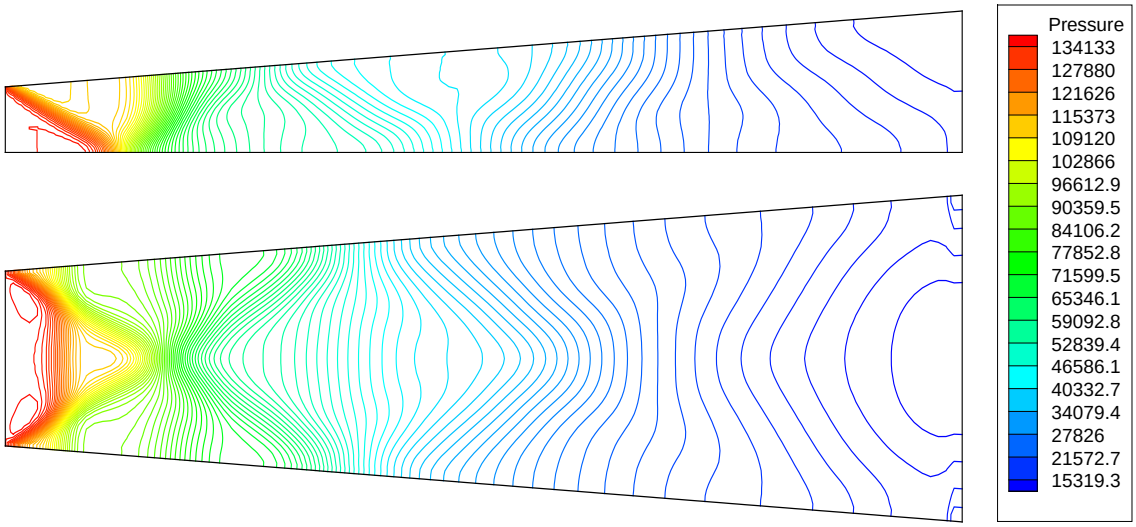

Figure 4.14 Case 3 - 2D inviscid contour lines: Pressure. (top: x-y midplane, bottom: x-z midplane)

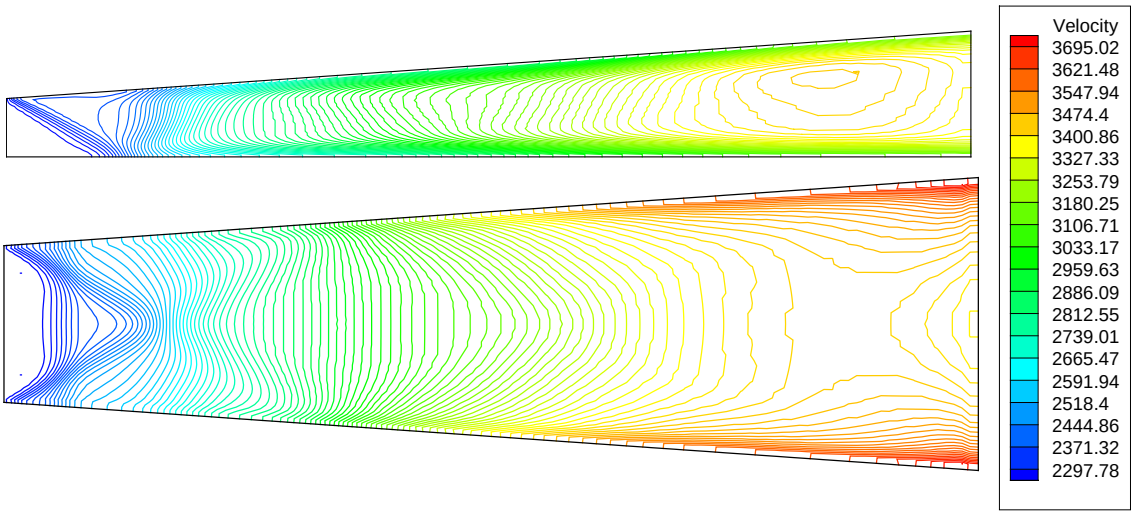

Figure 4.15 Case 3 - 2D inviscid contour lines: Velocity. (top: x-y midplane, bottom: x-z midplane)

4.2.2 Case 4: Inviscid Load Factor 1.2. Case 4 of this investigation used a load factor, $\mathcal{K}$, of 1.2. For this load factor, electrical potentials on the cathode and anode were set to ± 0.4549 respectively. This decrease in electrical potential produced a different Lorentz force vector field as shown in Figure 4.16. The vector plot is similar to the one in Figure 4.10, such as the inlet and exit effects caused by 'leakage' of the current around the electrodes. It is important to note where the Lorentz force transitions from accelerating to decelerating. In Case 4, this transition occurs earlier, approximately 60% of the accelerator length. This means that the MGD interactions with the flow have caused a larger decelerating region of the flow. In addition, the magnitude of the maximum Lorentz force has dropped 20% from 0.679 to 0.564. With a smaller accelerating region and a larger decelerating region, it is expected that the thrust produced by MGD will decrease from Case 3.

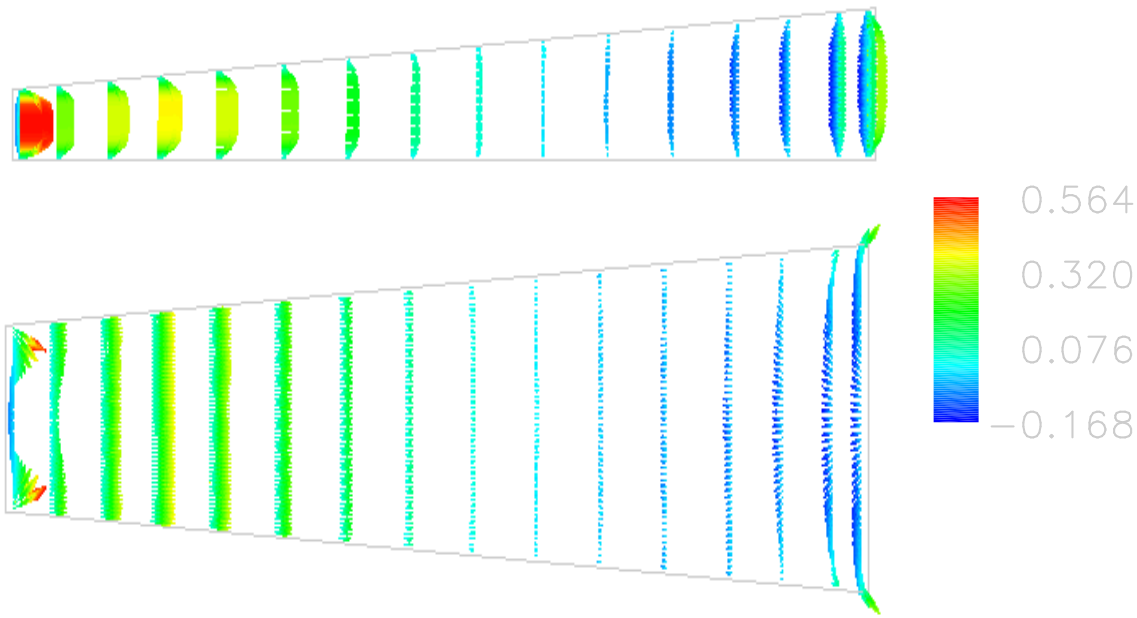

Figure 4.16 Case 4 - Lorentz vectors. (top: x-y midplane, bottom: x-z midplane)

The velocity contours for this MGD case are shown in Figure 4.17. Like Case 3, the decelerating Lorentz force causes the velocity to stall and then decrease although the geometry of the accelerator is still expanding. This decreasing velocity region of the flow is larger than the one for Case 3 shown in Figure 4.15.

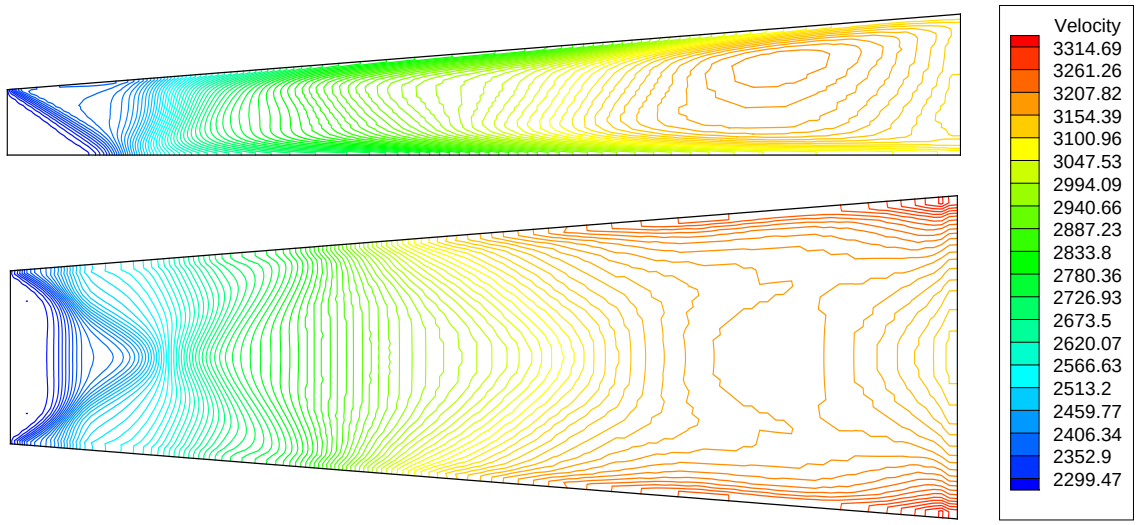

Figure 4.17 Case 4 - 2D inviscid contour lines: Velocity. (top: x-y midplane, bottom: x-z midplane)

The temperature contours shown in Figure 4.18 show little increase in maximum temperature, only 2% or 65K higher than the baseline in Case 1. The maximum temperature for Case 4 is 2957.5K, which unlike Case 3 is still within known material limits. As in Case 3, the area of highest temperature occurs along the electrodes where the accelerating Lorentz force is the largest.

4.2.3 Case 5: Inviscid Load Factor 1.8. A load factor of 1.8 used in Case 5 produced electric potential values of ± 0.6824 for the cathode and anode respectively. Figure 4.19 shows the direction of the Lorentz force, which ranges in magnitude from 0.893 in the accelerating direction to 0.186 in the decelerating direction. This is a 31.5% increase in the accelerating force from Case 3. In addition, the region of decelerating Lorentz force vectors is reduced when compared to Cases 3 and 4. This means that the flow is accelerating for a longer time, thus increasing flow velocity. Like the two previous cases, the highest magnitude of the Lorentz force is located in the first half of the accelerator.

The velocity contours in Figure 4.20 show the maximum velocity located at the walls near the exit is 50.4% greater than the maximum velocity in the baseline Case

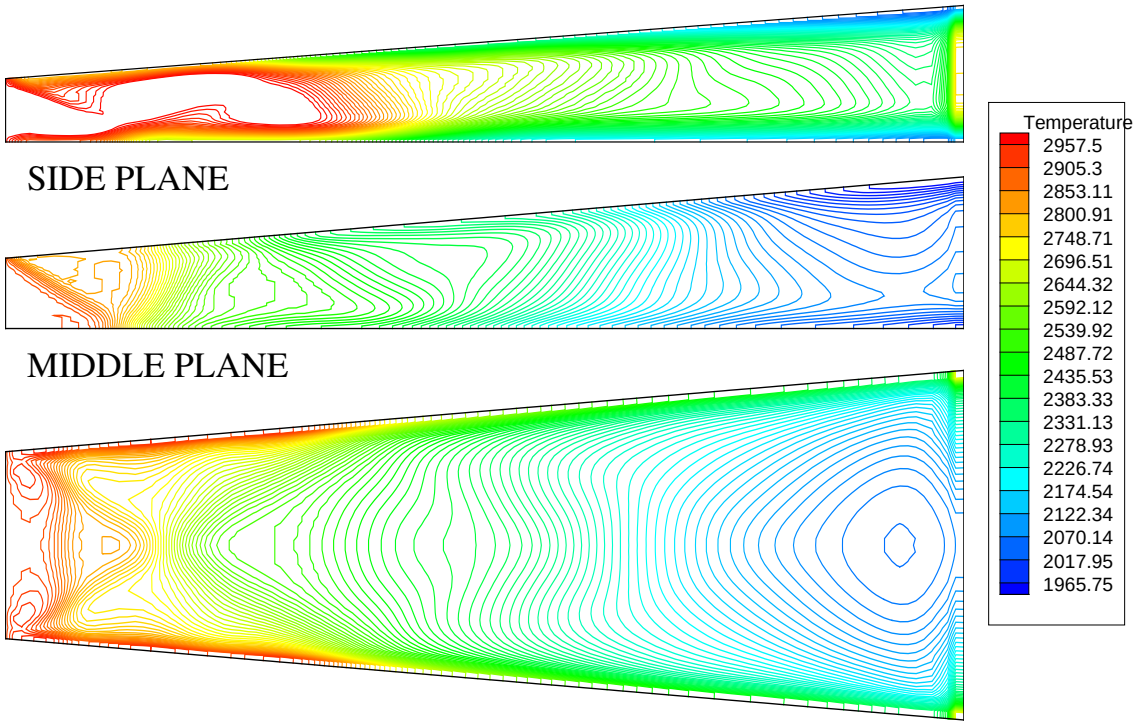

Figure 4.18 Case 4 - 2D inviscid contour lines: Temperature. (top: x-y side plane, middle: x-y midplane, bottom: x-z midplane)

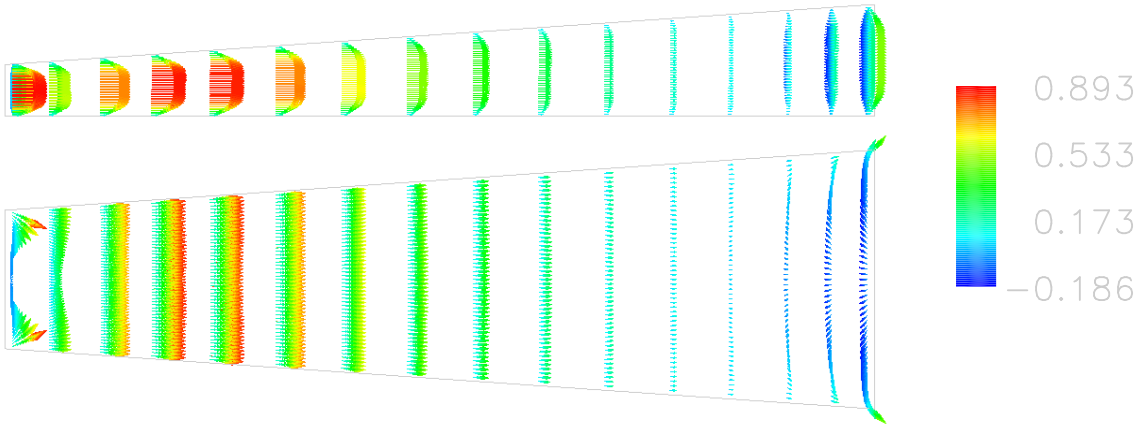

Figure 4.19 Case 5 - Lorentz vectors. (top: x-y midplane, bottom: x-z midplane)

1. In addition, the maximum velocity from Case 1 is achieved in only 30% of the accelerator length. Despite this acceleration, there is still a decelerating effect from the decelerating Lorentz force vectors in the mainstream flow near the accelerator exit.

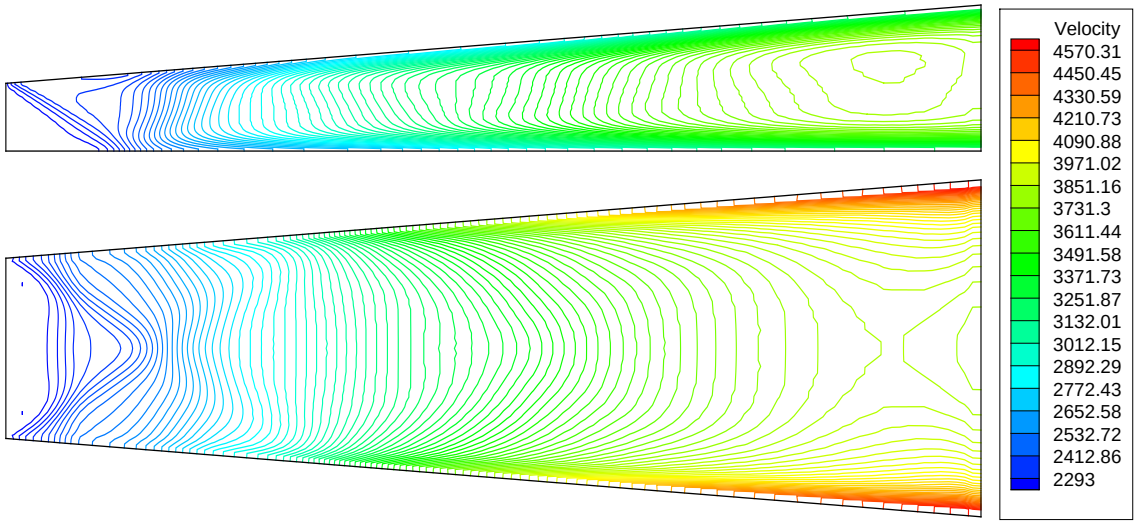

Figure 4.20 Case 5 - 2D inviscid contour lines: Velocity. (top: x-y midplane, bottom: x-z midplane)

The large increase in velocity, causes a large penalty in heating as shown by the temperature contours in Figure 4.21. The maximum temperature, located on the electrodes near the accelerator exit, reaches 5545K, 91.7% higher than in Case 1. This is due to greater Joule heating.

4.2.4 Case 6: Viscous Load Factor 1.4. The first viscous MGD case was solved using a load factor of 1.4. This load factor cased the electric potential to be set to ± 0.515 on the cathode and anode, respectively. The numerical solution from this electric potential and conductivity pattern from Figure 3.5 resulted in the Lorentz force vector plot in Figure 4.22. As shown, there is a large increase in the Lorentz force in the corners of the accelerator, reaching magnitudes of 29.8 as opposed to the maximum of 0.893 in the inviscid cases. In addition, there are

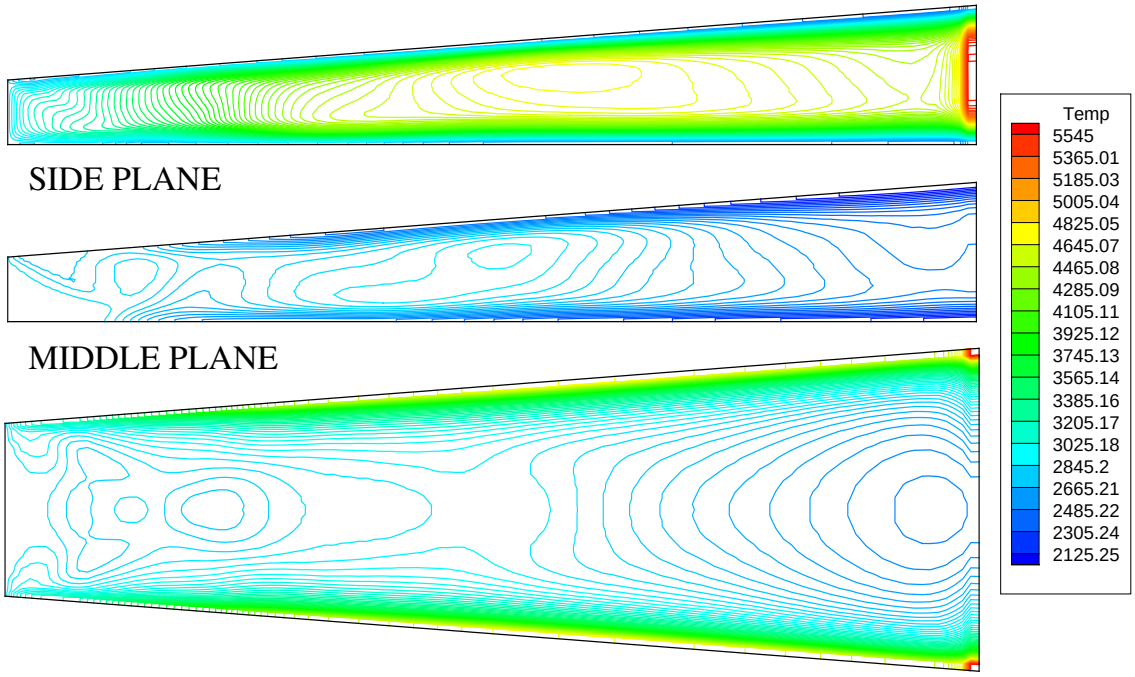

Figure 4.21 Case 5 - 2D inviscid contour lines: Temperature. (top: x-y side plane, middle: x-y midplane, bottom: x-z midplane)

also large decelerating Lorentz force vectors in the corners. However, these larger accelerations and decelerations occur where the velocity is essentially zero.

Despite the large Lorentz force vectors, the mainstream flow away from the corners is similar to the inviscid Lorentz force patterns. This is shown in Figure 4.23 which has many of the same features as Case 3 shown in Figure 4.10. The accelerating Lorentz force is greater in the first half of the accelerator and falls to zero in the same location as Case 3. The same inlet and exit characteristics are present including the decelerating Lorentz force in the aft region of the accelerator.

The larger Lorentz forces in the accelerator corners caused some flow features in Case 6 that differ from those in baseline Case 2. Figure 4.24 shows three dimensional contour plots for velocity magnitude and Mach number. Vortices form aft the accelerator inlet in each corner, characterized by increased velocity and temperature. Despite the large velocities in the corners, the Mach number drops in the corners compared to the baseline Case 2 due to increases in temperature. In comparison

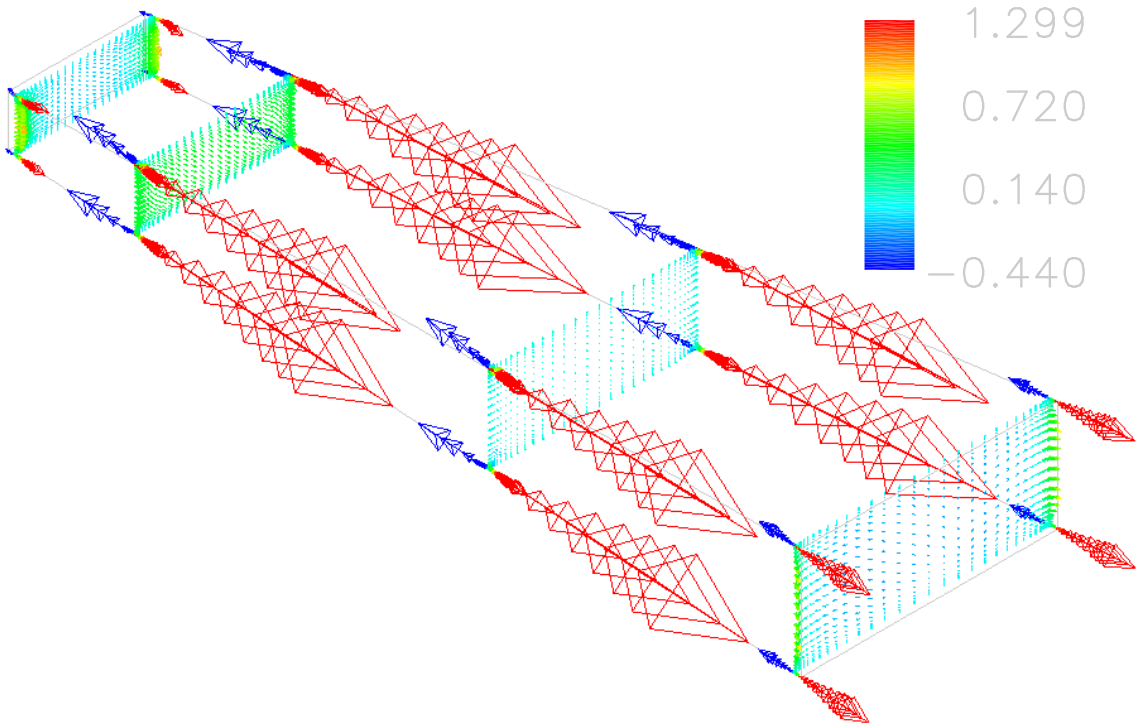

Figure 4.22 Case 6 - 3D Lorentz force vectors.

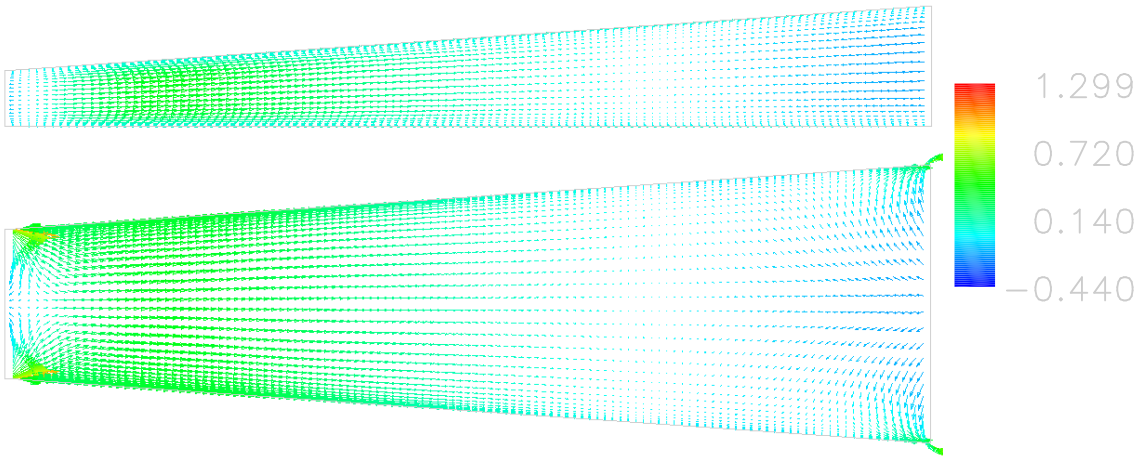

Figure 4.23 Case 6 - 2D Lorentz force vectors. (top: x-y midplane, bottom: x-z midplane)

with Figure 4.5, the flow in the corners is at a much lower mach number than the baseline case.

The temperature contours in the mainstream flow shown in Figure 4.26 show a representation of the temperature in the flow. As shown, the temperature gradients remain the largest near the electrode surfaces and the contours in the mainstream are not as uniform as in the baseline case. The temperature increases in the first portion of the accelerator before dropping as is expected in flow expansion. These changes in temperature are due to the energy interaction source term. Figure 4.25 shows the mainstream viscous flow structures. Like the inviscid MGD cases, an area of decelerating flow is seen near the accelerator exit as the decelerating Lorentz forces retard the flow.

4.2.5 Case 7: Viscous Load Factor 1.8. The second load factor investigated in the viscous flow regime is $\mathcal{K} = 1.8$ in Case 7. As shown in Figure 4.27, many of the same Lorentz force characteristics seen in Case 6 are also seen in Case 7. The boundary layer in the corners contain both large accelerating and decelerating Lorentz force vectors. Comparing Figure 4.27 to Figure 4.22, the magnitude of the Lorentz vectors are greater for the larger load factor. This is most apparent in the region just after the inlet where the flow is mainly characterized by accelerating vectors. The mainstream flow shows accelerating vectors similar to those found in Case 5, the inviscid case with the same load factor, shown in Figure 4.19. Figure 4.28 shows the mainstream Lorentz force vectors. Again the area of greatest accelerating Lorentz vectors is in the first half of the accelerator. Again, similar to Case 5, the area before the accelerator exit is characterized by decelerating Lorentz forces, which occur in approximately the same location. Lastly, the inaccuracies due to 'leakage' around the exit and inlet are visible.

Figure 4.29 shows the velocity magnitude and Mach number contours for the MGD viscous flow field. The same flow vortices seen in the corners in Case 6 appear

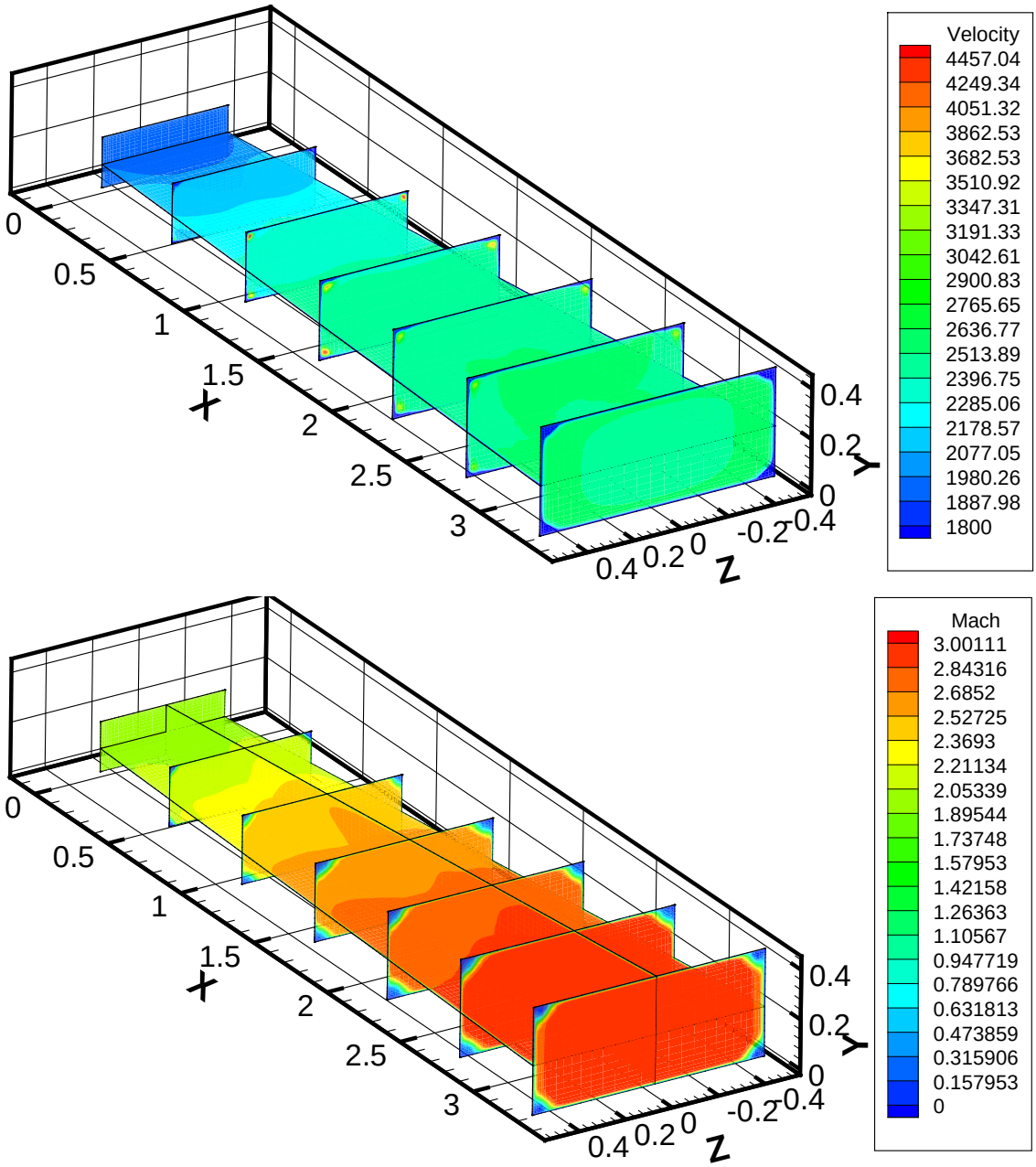

Figure 4.24 Case 6 - 3D flow field contours.

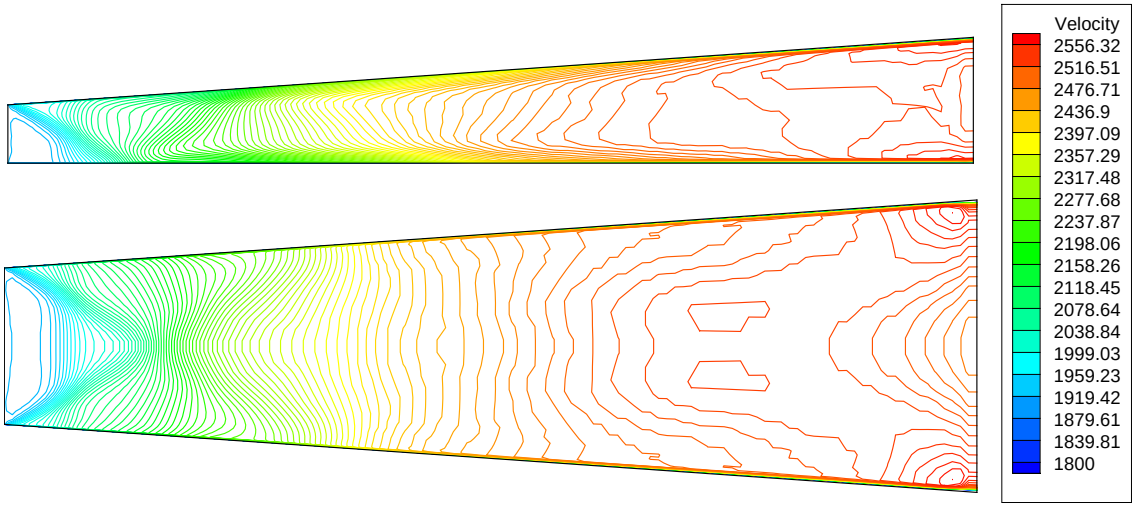

Figure 4.25 Case 6 - 2D viscous contour lines: Velocity. (top: x-y midplane, bottom: x-z midplane)

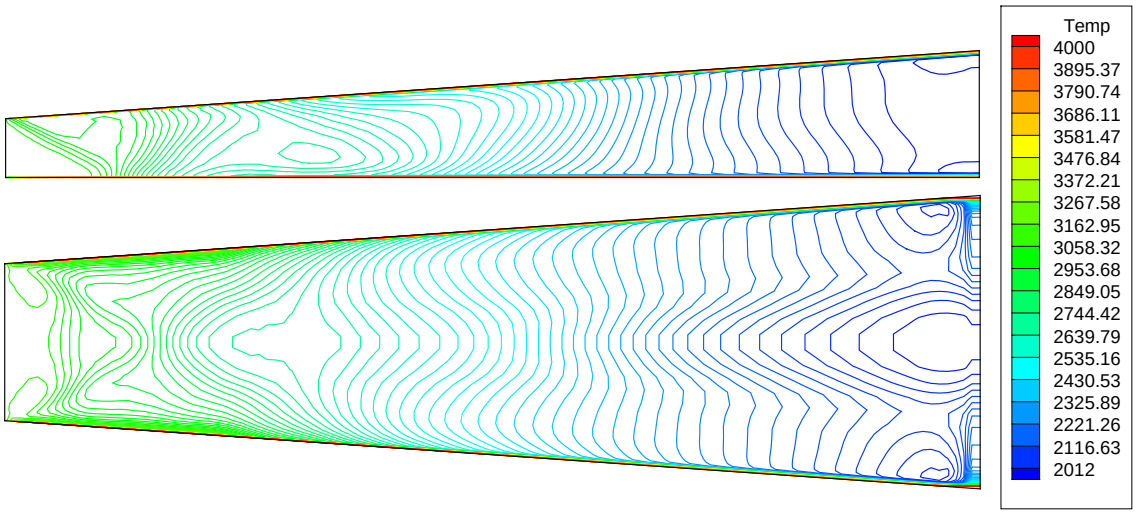

Figure 4.26 Case 6 - 2D viscous contour lines: Temperature. (top: x-y midplane, bottom: x-z midplane)

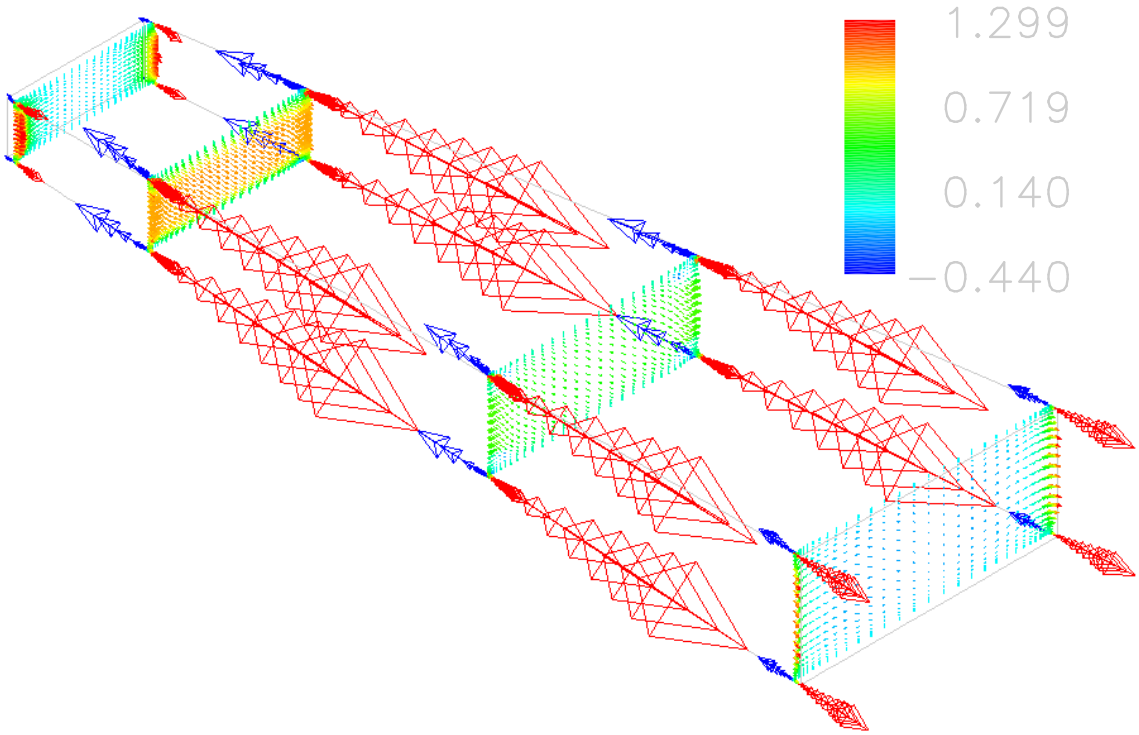

Figure 4.27 Case 7 - 3D Lorentz force vectors.

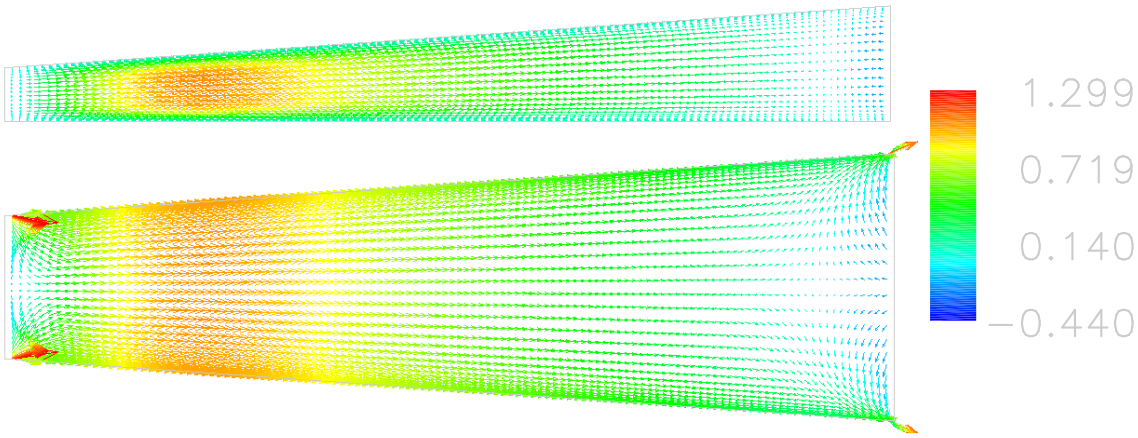

Figure 4.28 Case 7 - 2D Lorentz force vectors. (top: x-y midplane, bottom: x-z midplane)

in Case 7, but with higher velocity and temperature. The vortex structures are more developed and span a longer portion of the accelerator. Velocities in the corner vortices are 50% larger than in those in Case 6, and the temperature more than doubles in magnitude. The Mach number contour plot shows a larger subsonic region in the corners that grows down the length of the accelerator. These corner vortices were also seen by Gaitonde in his MGD acceleration results [7].

The mainstream flow properties in Figures 4.30 and 4.31 for velocity and temperature, respectively, agrees well with the results from Case 6. However,the change in load factor did have some effect. In comparison to Figure 4.25, the velocity magnitude has increased to 3001m/s although this is still 1.2 lower than the baseline viscous case. The velocity increases to a larger value earlier in the flow path with the 1.8 load factor, but as in the previous case, the velocity is again decelerated in the area near the exit with decelerating Lorentz forces.

The temperature contours shown in Figure 4.31 show a representation of the temperature in the flow. In comparison to Figure 4.7, the temperature has been significantly effected by MGD interactions. The temperature gradients near the electrode surfaces are very large, reaching over 4000K outside the boundary layer and increasing toward the surface. In the mainstream, the temperature again increases in the first portion of the accelerator before dropping as is expected in flow expansion.

4.3 MGD Results: Conductivity Pattern 2

The second conductivity pattern, shown in Figure 3.6, was used to investigate what effect conductivity had on the flow field and flow acceleration. The second pattern, designed to simulate seeding of the flow with ionized particles, has a non-dimensional conductivity of unity at the walls and falls towards zero in the mainstream. Case 8 investigates the effect of conductivity pattern 2 on inviscid flow using a load factor of 1.4.

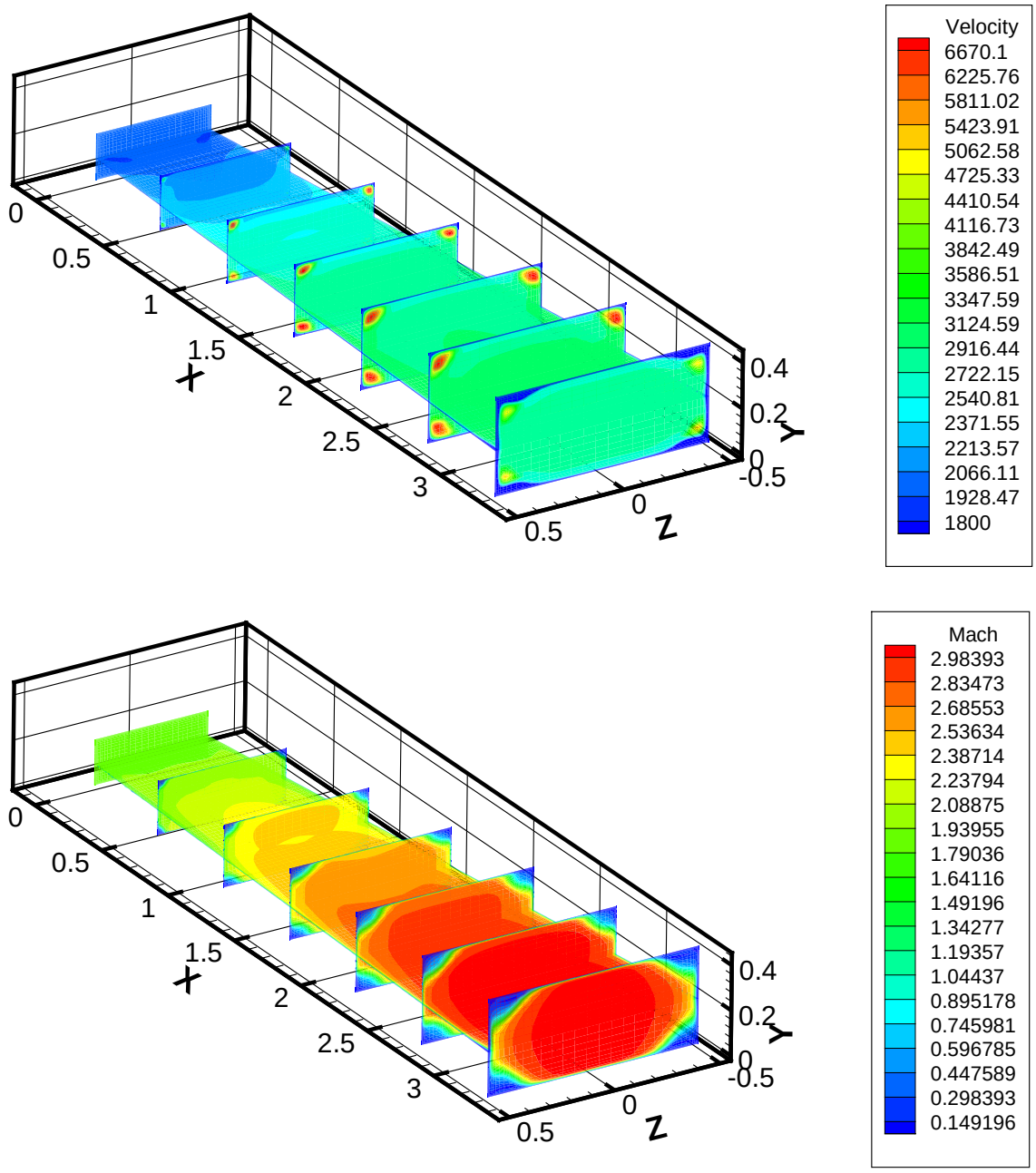

Figure 4.29 Case 7 - 3D flow field contours.

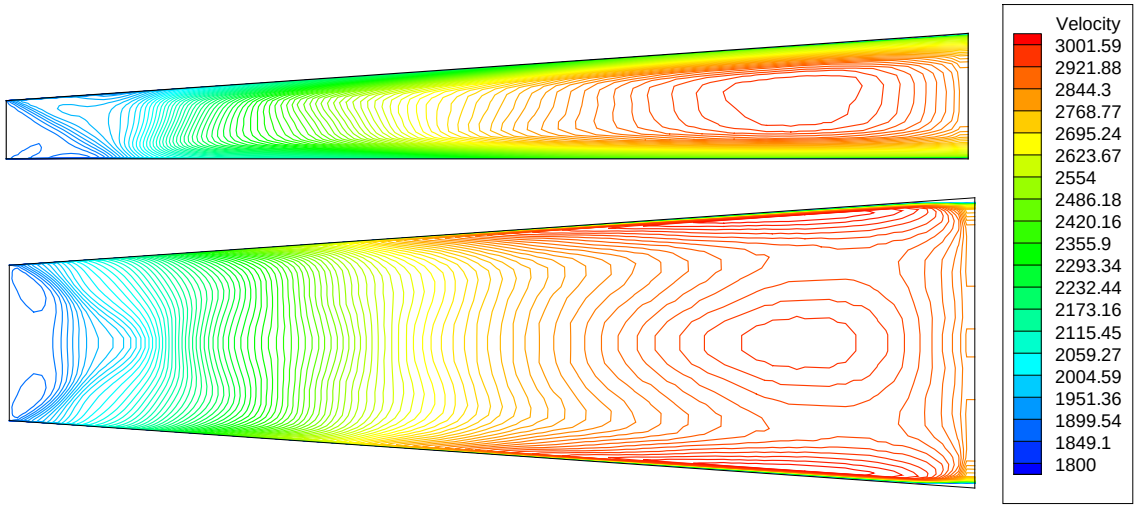

Figure 4.30 Case 7 - 2D viscous contour lines: Velocity. (top: x-y midplane, bottom: x-z midplane)

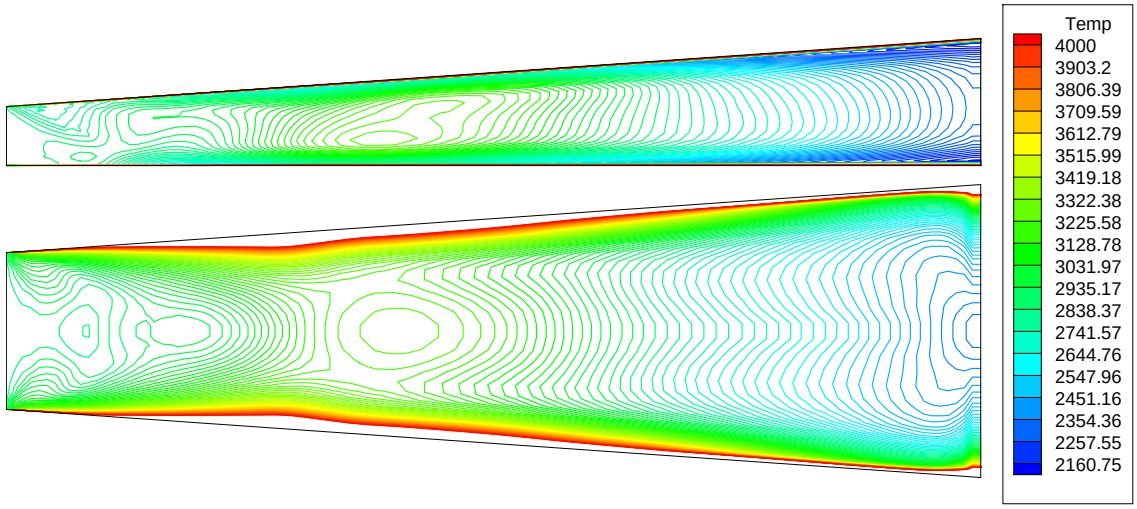

Figure 4.31 Case 7 - 2D viscous contour lines: Temperature. (top: x-y midplane, bottom: x-z midplane)

4.3.1 Case 8: Inviscid Load Factor 1.4. A load factor of 1.4 was used in Case 8 to determine the electric field. This load factor set the electric potential on the cathode and anode to ±0.5530, respectively, similar to Case 3. The Lorentz force vectors calculated for this case are shown in Figure 4.32. The area of largest accelerating Lorentz forces is along the electrode surface near the inlet. While part of this is due to the boundary conditions at the inlet causing 'leakage', it is also the area with the highest conductivity. The same is true at the corners located near the exit of the accelerator.

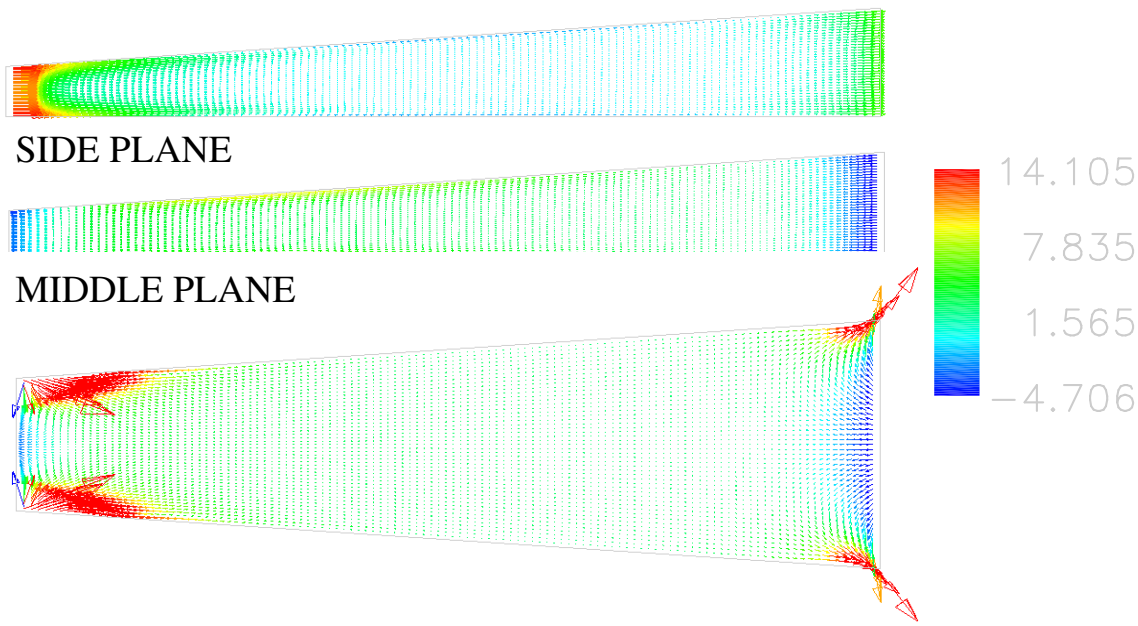

Figure 4.32 Case 8 - 2D Lorentz force vectors. (top: x-y side plane, middle: x-y midplane, bottom: x-z midplane)

Figure 4.33 shows scaled Lorentz force vectors for the x-z midplane of the accelerator. The Lorentz force in the mainstream flow is almost negligible. A result of the new conductivity pattern is decelerating Lorentz vectors along the walls in this midplane of the accelerator. Figure 4.33 shows the relative magnitudes of the accelerating and decelerating Lorentz forces along the wall. The first few cells near the wall show decelerating force vectors which rapidly transition to accelerating force vectors as the conductivity falls off in the mainstream.

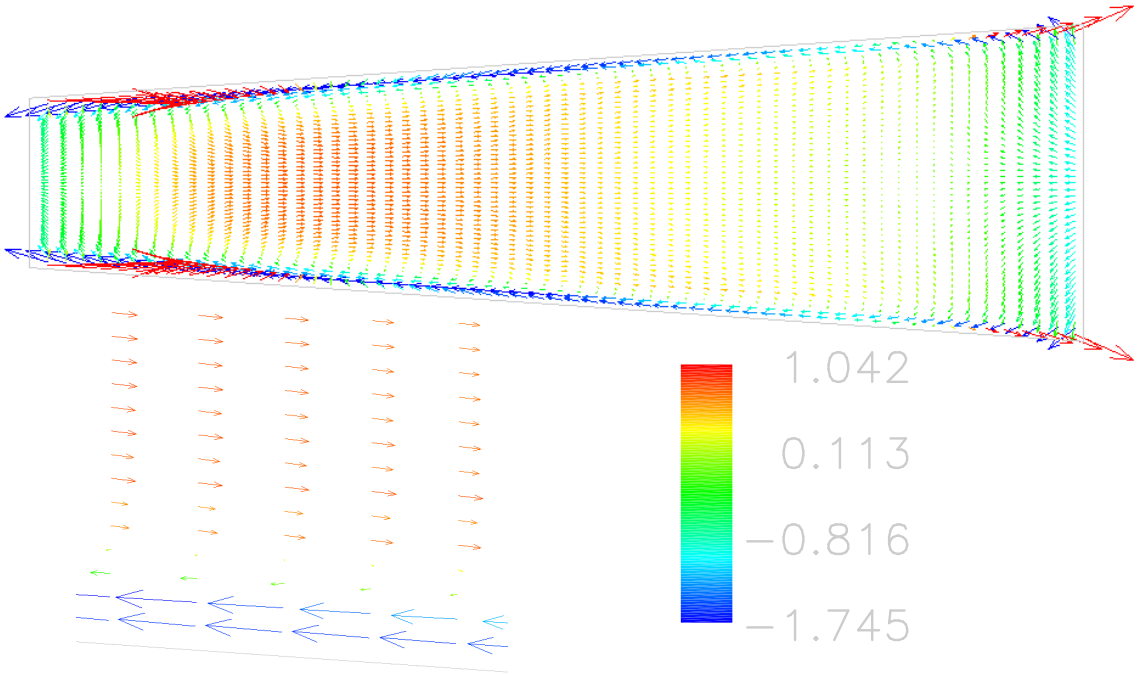

Figure 4.33 Case 8 - Scaled Lorentz force vectors and electrode wall profile. (top: x-z midplane, bottom: electrode wall profile)

The velocity magnitude contour plot shown in Figure 4.34 shows the concentration of high velocity in the corners near the accelerator exit. The maximum velocity in this case, however, is 29.2% lower than the maximum in the inviscid baseline Case 1. There are larger gradients near the inlet, and the same velocity deceleration caused by the decelerating Lorentz forces is shown near the exit.

The temperature contours in Figure 4.35 show the areas of high temperature for Case 8. These are located along the walls near the exit and inlet of the accelerator where the conductivity, again shown in Figure 3.6, is the greatest. Like many of the other MGD results, the temperature gradients near the inlet are larger than the baseline case, and there is a decrease in mainstream temperature before the exit.

4.4 Load Factor Effects

The load factor was varied in this study to examine its effect on flow properties. Three inviscid cases for conductivity pattern 1 with different load factors produced

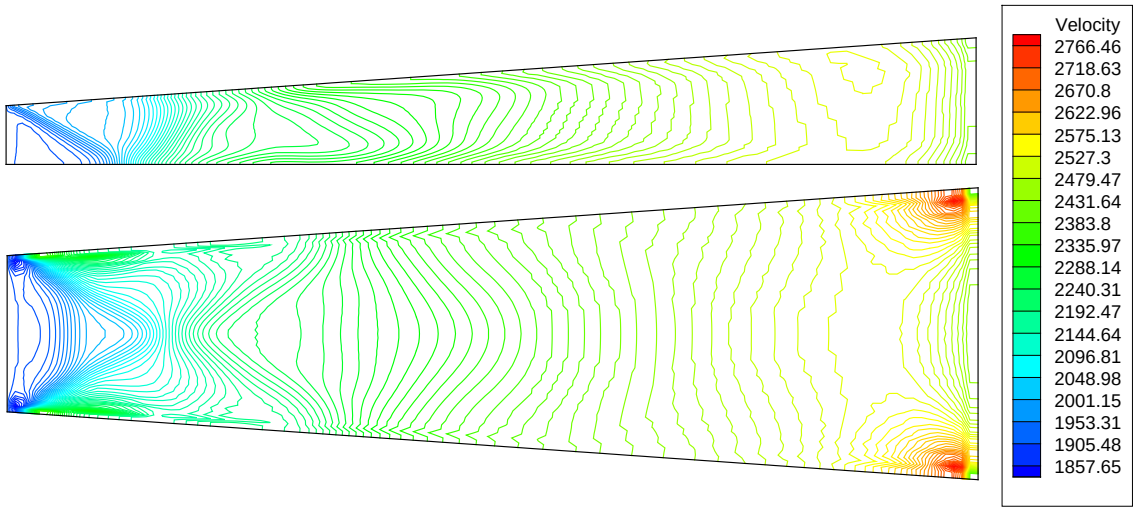

Figure 4.34 Case 8 - 2D inviscid contour lines: Velocity. (top: x-y midplane, bottom: x-z midplane)

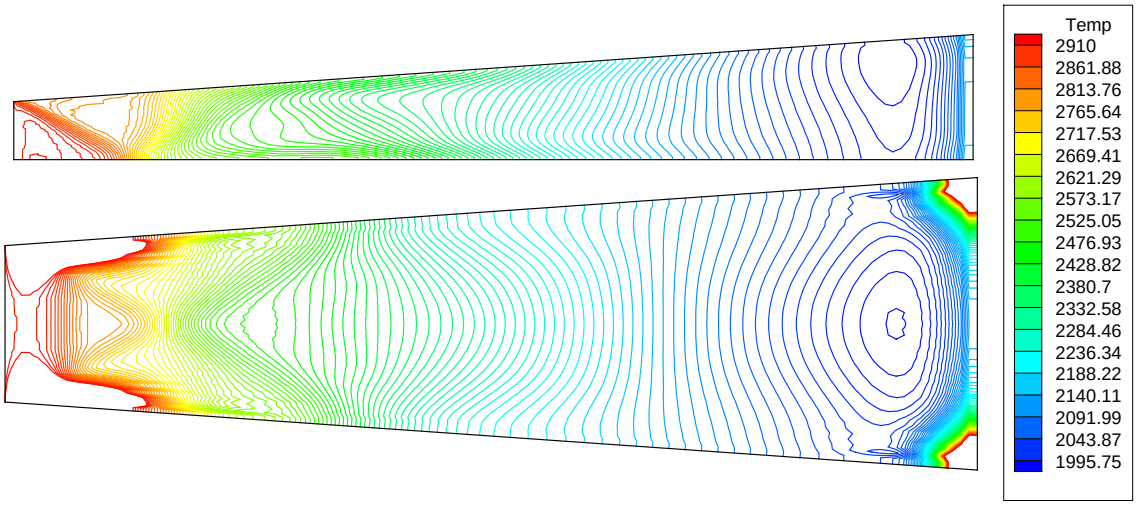

Figure 4.35 Case 8 - 2D inviscid contour lines: Temperature. (top: x-y midplane, bottom: x-z midplane)

different Lorentz force vector plots, shown together in Figure 4.36. The dashed line placed across each vector plot symbolizes the location where the Lorentz force changed from an accelerating force to a decelerating force. The region of decelerating Lorentz force near the exit has to do with how the Lorentz force is calculated. The Lorentz force is $(\vec{j} \times \vec{B})$ where $\vec{j} = \sigma(\vec{E} + \vec{V} \times \vec{B})$. The reference velocity used in this study to set electrical potential was taken halfway through the accelerator. As the flow accelerates beyond this value, the $\vec{V} \times \vec{B}$ term which creates a decelerating force becomes larger than the $\vec{E}$ term which creates an accelerating force. As the load factor is increased, the $\vec{E}$ term dominates over more of the accelerator. This increases the axial distance where the flow is in the presence of an accelerating force and flow velocity.

4.5 Thrust

The overall thrust of the MGD accelerator was assessed by calculating the stream thrust function at both the inlet and exit of the accelerator/nozzle as described in Section 3.2. The difference of the inlet and exit stream functions is the force exerted on the flow by both the MGD interactions and the expansion of the flow through the accelerator/nozzle. Table 4.1 summarizes the eight test cases, their parameters, and the force exerted on the flow compared to the baseline cases.

For both the viscous and inviscid results, the greatest increase in axial force exerted on the flow is with a load factor of 1.8. The greatest increase in axial force change from the baseline was the viscous case which increase the axial force on the flow more than two times the baseline value. As the load factor decreases, so does the percent increase from the baseline cases. The viscous flow regime with a load factor of 1.4 showed the least increase in specific thrust, increasing less than 1%.

Increasing load factor in both flow regimes greatly increased the specific thrust, but also increased Joule heating associated with the energy interaction term. This resulted in higher temperatures through the flow field as higher load factors were

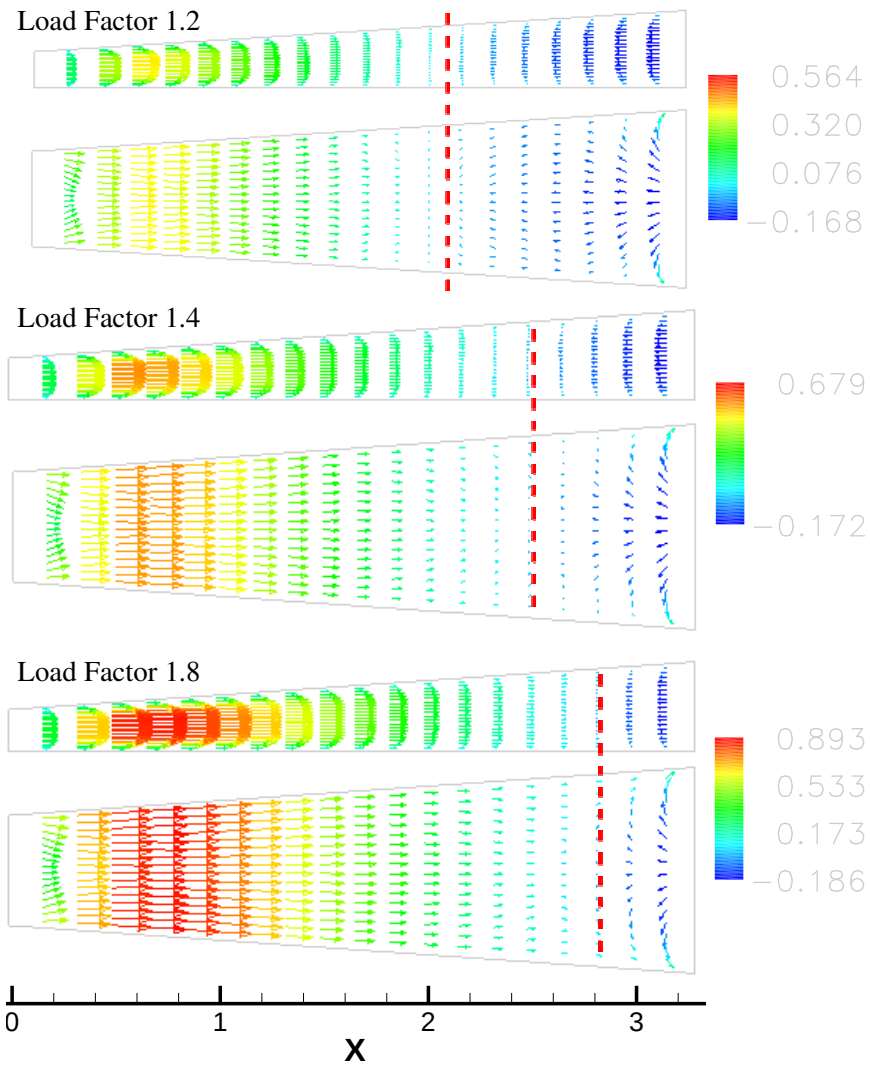

Figure 4.36 Lorentz vectors for Cases 3, 4 and 5.

Table 4.1 Summary of Test Case Exit Plane Results.

Case Number	Flow Regime	Load Factor ($\mathcal{K}$)	Conductivity Pattern	ΔSa (m/s)	Δ from Baseline
1	Inviscid	none	none	5355.02	—
2	Viscous	none	none	5273.73	—
3	Inviscid	1.4	1	8924.55	66.7%
4	Inviscid	1.2	1	6424.70	20.0%
5	Inviscid	1.8	1	13610.27	154.2%
6	Viscous	1.4	1	5318.66	0.8%
7	Viscous	1.8	1	17192.76	226.0%
8	Inviscid	1.4	2	5465.01	2.1%

implemented. In the viscous cases, the specific thrust more than doubled between load factors of 1.4 and 1.8, but so did the temperature. Viscous cases also appear to be more sensitive to the load factor than the inviscid cases. An increase in load factor from 1.4 to 1.8 increased specific thrust approximately 90% in inviscid cases as opposed to over 200% in the viscous cases.

Although load factor seems to play a larger role in this study, conductivity also had significant effect on thrust. The second conductivity pattern, representing a seeded flow, had little increase in the axial force exerted on the flow, increasing only 2.1% from the baseline. Conductivity pattern 1 for the same load factor resulted in a 66% increase showing much more promise in future research. Even at a smaller load factor of 1.2, conductivity pattern 1 showed 10 times the improvement in thrust over conductivity pattern 2 at a load factor of 1.4.

5. *Conclusions*

The effect of MGD interactions on flow acceleration and thrust in a scramjet accelerator/nozzle have been examined numerically at a free-stream flight condition of Mach 8. The parameters of conductivity pattern and load factor were varied in both inviscid and viscous flow regimes with the intent of increasing the axial force exerted on the flow through the accelerator. Increases in axial force for MGD solutions were compared to the non-MGD solution to determine the what effect the parameters have on the thrust. For the configurations investigated in this study, the mass flow specific thrust increase ranged from negligible to as much as 226%. The viscous case using a load factor of 1.8 and an electron beam type conductivity was most effective in increasing axial force. The inviscid case using the same load factor and conductivity showed the most improvement for the inviscid cases, increasing axial force 154% from the inviscid baseline.

The conductivity pattern simulating seeding of the flow with charged particles was implemented in an inviscid flow solution, but showed a negligible increase in specific thrust, increasing only 2.1% above the baseline inviscid solution. The electron beam pattern modeled in conductivity pattern 1 demonstrated a greater capability to accelerate the flow and increase specific thrust.

Flow acceleration using MGD is not without tradeoffs. Load factor increases show significant rise in temperature across the accelerator. Although higher load factors increase axial force, they also increase Joule heating due to the energy interaction term and reduce engine efficiency. Additional material advancements are required to withstand the high temperatures encountered in the flow path. Engine efficiency also drives a tradeoff between increased thrust and the energy spent ionizing and accelerating the flow.

The continuous electrode design caused some unique flow structures. The 'leakage' mentioned in Section 4.2 and 4.3 is a result of the boundary conditions

around the electrode. The side walls have a constant electrical potential boundary condition, and the top and bottom walls are electromagnetic insulators. The inlet and outlet have no restrictions on the current. These boundary conditions cause a 'leakage' of the current at the inlet and exit. One possible solution to this discrepancy would be to include on the side wall a border around the electrode with an insulator boundary condition. This would reduce the 'leakage' flow effects caused by the current boundary conditions.

Future research into the area of MGD flow acceleration is required to determine optimum operating conditions for hypersonic flow. Of importance are the electrode configurations and conductivity patterns, and load factors which have significant impact on flow structures. In addition, research into the efficiency of flow acceleration using various load factors and conductivity patterns is also needed before this research can be implemented in a realistic design.

Bibliography

1. Brichkin, D.I., Kuranov A.L. and E.G. Sheikin. *Scramjet with MHD Control Under "AJAX" Concept. Physical Limitations.*. AIAA Paper 2001–0381, January 2001.

2. Burakhanov, B.M., Likhachev A.P. Medin S.A Novikov V.A. Okunev V.I. Rickman V. Zeigarnik V. "Advancement of Scramjet Magnetohydrodynamic Concept," *Journal of Propulsion and Power*, *17*(6):1247–1252 (November 2001).

3. Davis, D.L. *Scramjet Fuel Mixing Enhancement by Cross-Stream Pressure Gradients*. AIAA Paper 1993–2139, June 1993.

4. Dornheim, M.A., "X-43 Flight Test Indicates Thrust is Greater than Drag," *A Breath of Fast Air* Aviation Week & Space Technology Website, (2004). 21 Apr 2004 http://www.aviationnow.com/avnow/news/ channel_awst_story.jsp?id=news/04054wna.xml.

5. Earp, B. E. *Magnetogasdynamic Flow Control of a Mach Reflection*. MS thesis, Airforce Institute of Tecnology, WPAFB, OH, March 2004.

6. Gaitonde, D. V. *Development of a Solver for 3-D Non-ideal Magnetogasdynamics*. AIAA Paper 99–3610, June 1999.

7. Gaitonde, D. V. *Three-Dimensional Flow-Through Scramjet Simulation with MGD Energy- Bypass*. AIAA Paper 2003–0172, January 2003.

8. Gaitonde, D. V. and J. Poggie. *Simulation of Magnetogasdynamic Flow Control Techniques*. AIAA Paper 2000–2326, June 2000.

9. Gaitonde, D. V. and J. Poggie. *An Implicit Technique for 3-D Turbulent MGD with the Generalized Ohms Law*. AIAA Paper 2001–2736, June 2001.

10. Gaitonde, D. V. and J. Poggie. *Elements of a Numerical Procedure for 3-D MGD Flow Control Analysis*. AIAA Paper 2002–0198, January 2002.

11. Gaitonde, D. V. and J. Poggie. *Preliminary Analysis of 3-D Scramjet Flowpath with MGD Control*. AIAA Paper 2002–2134, May 2002.

12. Heiser, W.H. and D.T. Pratt. *Hypersonic Airbreathing Propulsion*. Washington, DC: American Institute of Aeronautics and Astronautics, 1994.

13. Hirsch, C. *Numerical Computation of Internal and External Flows, Volume 2*. John Wiley and Sons, 1990.

14. Hughes, W. F. and F. J. Young. *The Electromagnetodynamics of Fluids* (Reprint Edition). Malabar, FL: Robert E. Krieger Publishing Company, 1989.

15. "Center for Hypersonics - Hyshot Scramjet Test Program," *Hyshot: A Univeristy of Queensland Initiative* Univeristy of Queensland Website, (2003). 21 Apr 2004 http://www.mech.uq.edu.au/hyper/hyshot/.

16. Kuranov, A. and E. Sheikin. *The Potential of MHD Control for Improving Scramjet Performance*. AIAA Paper 99–3535, June 1999.

17. Kuranov, A. and E. Sheikin. *The Potentialities of MHD Control for Improving Scramjet Performance*. AIAA Paper 99–4969, January 1999.

18. Kuranov, A. and E. Sheikin. *MHD Control on Hypersonic Aircraft under "AJAX" Concept. Possibilites of MHD Generator*. AIAA Paper 2002–0490, January 2002.

19. Kuranov, A. and E. Sheikin. *Scramjet with MHD Bypass Under "AJAX" Concept.*. AIAA Paper 2004–1192, January 2004.

20. Kuranov, A.L., Kuchinsky V.V. and Sheikin E.G. *Scramjet with MHD Control Under "AJAX" Concept. Requirements for MHD Systems.*. AIAA Paper 2001–2881, June 2001.

21. Lichford, R. J. and J. W. Cole. "Thermodynamic Cycle Analysis of Magnetohydrodynamic-Bypass Hypersonic Airbreathing Engines," *J. Propulsion*, *17*(2):477–480

22. Macheret, S.O., Shneider M.N. and R.B. Miles. *Potential Performance of Supersonic MHD Power Generators*. AIAA Paper 2001–0795, January 2001.

23. Macheret, S.O., Shneider M.N. and R.B. Miles. "Magnetohydrodynamic Control of Hypersonic and Scramjet Inlets Using Electron Beam Ionization," *AIAA Journal*, *40*(1):74–81 (January 2002).

24. Macheret, S.O., Shneider M.N. and R.B. Miles. *Scramjet Inlet Control of Off-Body Energy Addition: A Virtual Cowl*. AIAA Paper 2003–0032, January 2003.

25. Mehta, U.B., Bogdanhoff D.W. and C. Park. *A Perspective on a Combined Magneto-Hydrodynamic-Scramjet Engine*. ISABE Paper 2001–1231, September 2001.

26. Mehta, U. B. "Strategy for Developing Air-Breathing Aerospace Planes," *Journal of Aircraft*, *33*(2):377–385 (March 1996).

27. Meyer, R., McEldowney B. Chintala N. Palm P. Adamovich I. *Experimental Studies of Plasma Assisted Ignitioand MHD Supersonic Flow Control*. AIAA Paper 2003–0873, January 2003.

28. Park, C. and D. Bogdanoff. "Theoretical Performance of Frictionless Magnetohydrodynamic-Bypass Scramjets," *Journal of Propulsion and Power*, *17*(3):591–598 (May 2001).

29. Turchak, A., Kuranov A. Korabelnikov A. Kuchinsky V. and E. Sheikin. *Hypersonic Technologies of the "AJAX" Concept.*. AIAA Paper 2002–5184, September 2002.

30. "Men of the X-1," *Faster Than Sound* NOVA online Website, (1997). 29 Apr 2004 http://www.pbs.org/wgbh/nova/barrier/men.html.

31. "Scramjet experiment soars off California coast," *Spaceflight Now* Spaceflight Now Website, (2004). 21 Apr 2004 http://www.spaceflightnow.com/news/n0403/27x43a/.

Vita

Ensign Brian H. Harrington was born in Los Gatos, CA. He was raised in San Jose, CA and graduated from Del Mar High School in 1999. He entered undergraduate studies at the United States Naval Academy in Annapolis, MD, where he graduated with a Bachelor of Science degree in Aeronautical Engineering and was commissioned in May of 2003.

In June 2003, he entered the Aeronautical Engineering program at the Graduate School of Engineering and Management, Air Force Institute of Technology. Upon graduation, he will be assigned to the Aviation Pre-flight Indoctrination program at NAS Pensacola, FL, where he will begin training to become a Naval Aviator.

REPORT DOCUMENTATION PAGE

Form Approved
OMB No. 0704–0188

The public reporting burden for this collection of information is estimated to average 1 hour per response, including the time for reviewing instructions, searching existing data sources, gathering and maintaining the data needed, and completing and reviewing the collection of information. Send comments regarding this burden estimate or any other aspect of this collection of information, including suggestions for reducing this burden to Department of Defense, Washington Headquarters Services, Directorate for Information Operations and Reports (0704–0188), 1215 Jefferson Davis Highway, Suite 1204, Arlington, VA 22202–4302. Respondents should be aware that notwithstanding any other provision of law, no person shall be subject to any penalty for failing to comply with a collection of information if it does not display a currently valid OMB control number. **PLEASE DO NOT RETURN YOUR FORM TO THE ABOVE ADDRESS.**

1. REPORT DATE *(DD–MM–YYYY)*	2. REPORT TYPE	3. DATES COVERED *(From — To)*
04–05–2004	Master's Thesis	Jul 2003 – Jun 2004

4. TITLE AND SUBTITLE

MAGNETOGASDYNAMIC FLOW ACCELERATION IN A SCRAMJET NOZZLE

5a. CONTRACT NUMBER

5b. GRANT NUMBER

5c. PROGRAM ELEMENT NUMBER

6. AUTHOR(S)

Harrington, Brian H., Ensign, USN

5d. PROJECT NUMBER

2003–014

5e. TASK NUMBER

5f. WORK UNIT NUMBER

7. PERFORMING ORGANIZATION NAME(S) AND ADDRESS(ES)

Air Force Institute of Technology
Graduate School of Engineering and Management
2950 Hobson Way
WPAFB OH 45433-7765

8. PERFORMING ORGANIZATION REPORT NUMBER

AFIT/GAE/ENY/04-J03

9. SPONSORING / MONITORING AGENCY NAME(S) AND ADDRESS(ES)

AFOSR/NA
Dr. John Schmisseur
801 N. Randolph Street, Rm 732
Arlington VA 22203-1977 (703) 696–6962

10. SPONSOR/MONITOR'S ACRONYM(S)

11. SPONSOR/MONITOR'S REPORT NUMBER(S)

12. DISTRIBUTION / AVAILABILITY STATEMENT

APPROVAL FOR PUBLIC RELEASE; DISTRIBUTION IS UNLIMITED.

13. SUPPLEMENTARY NOTES

14. ABSTRACT

The effect of magnetogasdynamic (MGD) interactions on flow acceleration and thrust in a scramjet accelerator/nozzle are examined numerically at a free-stream flight condition of Mach 8. The parameters of conductivity pattern and load factor are varied in both inviscid and viscous flow regimes with the intent of increasing axial force exerted on the flow through a scramjet accelerator. The numerical code solves the Navier-Stokes equations with additional source terms for the MGD forces and energy interactions. An accelerating Lorentz force is applied to the flow resulting from a constant magnetic field and an electric field produced by two continuous side wall electrodes. The specific thrust across the accelerator/nozzle is improved in the MGD solutions over the non-MGD solutions when the load factor is increased and an electron beam type ionization pattern is used. The largest increase in specific thrust is observed in viscous and inviscid flow regimes with a load factor of 1.8 producing 226% and 154% thrust increases, respectively. Flows showing increases in specific thrust with higher load factors also show significant increases in temperature due to the energy interaction term.

15. SUBJECT TERMS

Magnetogasdynamics; Flow Control; Flow Acceleration; Scramjet Nozzle; MGD Accelerator; Plasma

16. SECURITY CLASSIFICATION OF:			17. LIMITATION OF ABSTRACT	18. NUMBER OF PAGES	19a. NAME OF RESPONSIBLE PERSON
a. REPORT	b. ABSTRACT	c. THIS PAGE			Richard J. McMullan, Maj, USAF (ENY)
U	U	U	UU	83	19b. TELEPHONE NUMBER *(include area code)* (937)255–3069, Richard.Mcmullan@afit.edu

Standard Form 298 (Rev. 8–98)
Prescribed by ANSI Std. Z39.18